

## O–Cu(001): II. VLEED QUANTIFICATION OF THE FOUR-STAGE $\text{Cu}_3\text{O}_2$ BONDING KINETICS

CHANG Q. SUN

*School of Electrical and Electronic Engineering,  
Nanyang Technological University, Singapore 639798  
ecqsun@ntu.edu.sg*

Received 15 March 2001

Further to the previous part [*Surf. Rev. Lett.* **8**(3/4), 367 (2001)], this part deals with VLEED numerical quantification of the  $\text{Cu}_3\text{O}_2$  bond-forming kinetics on the Cu(001) surface. Besides the solution-number certainty that has been ensured, the modeling exercises have enabled the full capacity of VLEED to be explored, revealing that the bond geometry and the elastic potential define the shapes of the VLEED fine-structure features while the inelastic potential contributes to the absolute intensity. VLEED, covering the valence band in energy, is found to be able to collect nondestructive information from the top atomic layer, as the inelastic damping dominates in this region. Except for the bond geometry, dislocation of a single atom in the unit cell produces no feature that can match the VLEED spectral change, indicating the essentiality of the parametrization techniques developed. It is the right premise that it has enabled the four-stage O–Cu(001) reaction kinetics, revealed by VLEED, to be quantified as the evolution of the  $\text{CuO}_2$  to the  $\text{Cu}_3\text{O}_2$ . In addition, it is revealed that annealing provides disturbance rather than driving force strengthening the bond energy. Therefore, formulation in terms of bond making and its consequence on the behavior of atoms and valence electrons, and the corresponding parametrization, are demonstrated to be able to correctly reflect the real process of reaction and the correlation of the parameters as well as their natural link to the observations using LEED, STM and PES, or equivalent approaches.

<b>1</b>	<b>Introduction</b> . . . . .	<b>704</b>
<b>2</b>	<b>Further Justification</b> . . . . .	<b>704</b>
	2.1 Uniqueness of solutions . . . . .	704
	2.2 Capacity and reliability of VLEED . . . . .	708
<b>3</b>	<b>Angle-Resolved VLEED</b> . . . . .	<b>712</b>
	3.1 VLEED profiles . . . . .	713
	3.2 Sharp features: Brillouin zones and energy bands . . . . .	713
	3.3 Fine structures: bond geometry, DOS and 3D SPB . . . . .	715
<b>4</b>	<b>Inner Potential and Work Function</b> . . . . .	<b>717</b>
	4.1 Findings . . . . .	718
	4.2 Possible mechanisms . . . . .	718
<b>5</b>	<b>Exposure-Resolved VLEED</b> . . . . .	<b>721</b>
	5.1 VLEED data: four-stage reaction kinetics . . . . .	721
	5.2 Geometrical sensitivity . . . . .	721
	5.3 $\text{Cu}_3\text{O}_2$ bonding and band-forming kinetics . . . . .	723
	5.4 Summary . . . . .	725
<b>6</b>	<b>Aging and Annealing Effect</b> . . . . .	<b>726</b>
	6.1 Time-resolved VLEED data . . . . .	726

6.2 Dehybridization of oxygen . . . . .	726
6.3 Precursor confirmation . . . . .	728
<b>7 Summary . . . . .</b>	<b>731</b>
<b>Acknowledgments . . . . .</b>	<b>732</b>
<b>Appendix . . . . .</b>	<b>732</b>
<b>References . . . . .</b>	<b>733</b>

## 1. Introduction

In the first part,<sup>1</sup> we have described the model of oxidation bonding and incorporated it into the identities revealed by STM, STS, PES and LEED from the O–Cu(001) surface. Moreover, the model and the numerical treatment (in terms of bond geometry and the parametrized SPB) have minimized the numerical efforts because of the physical constraints applied to the parametrization of bond geometry and the SPB. Section 2 of this part shows that the parametrization also ensures the uniqueness of the number of solutions. There exist indeed correlations between the parameters, which give rise to multiple numerical solutions. VLEED-sensitivity examination revealed that adjusting the bond parameters can produce features that match the measured spectral change; in contrast, adjusting the atomic positions produces no match of the spectral features, evidencing the correctness of parameter assignment. Sections 3–6 demonstrate the outcomes of decoding a series of kinetic VLEED I–E spectra from the O–Cu(001) surface. Quantitative information is gained about the change of bond geometry, the valence DOS, the anisotropy and uniformity of the SPB, the work-function and inner-potential reduction during the reaction. A consistent quantification of the four-stage O–Cu(001) bonding kinetics in terms of evolution of the bond geometry and the valence DOS, particularly the DOS features of nonbonding states, provides further robust evidence for the modeling exercises.

## 2. Further Justification

### 2.1. Uniqueness of solutions

It is known that independent treatment of the crystal and electrical parameters in simulation of diffraction could lead to solution uncertainty,<sup>2</sup> because the diffraction intensity depends on the arrangement of scattering centers with different cross-sections.

The geometrical arrangement determines the phase change of diffracted beams and the cross-section, depending on the effective charges of the scattering centers, determines the amplitude of the diffracted waves. Therefore, reaction with charge transfer and SPB modification will lead to solution uncertainty in the VLEED energy range, particularly if we treat the correlated parameters independently. Here we show that the infinite solutions due to the independent treatment of the correlated SPB parameters can be unified by the new approach, and hence the parametrization implemented is essential.

It will be verified that  $z_0$  correlates with  $\lambda$  by the integration of  $\text{Re} V(z, z_0, \lambda)$  being a constant. This indicates that the integration of  $\text{Re} V(z, z_0, \lambda)$  is more important than the particular shape of  $\text{Re} V(z, z_0, \lambda)$ , and even the exact values of the individual parameters included, in determining the beam reflectivity.

In the practice of verifying the uniqueness of solutions, all the SPB parameters were treated as independent, as in conventional wisdom. Inspection of the uniqueness of solutions was conducted at several energy values. Except for a selected pair of SPB parameters, for example  $z_0$  and  $\lambda$ , the structural and other SPB parameters were kept unchanged. Calculation of the VLEED spectrum collected at  $43.5^\circ$  azimuth was repeated by using as the next iteration the output of the initial  $z_0(E)$  calculation of this spectrum. All other parameters were automatically generated with the SPB functions as given in Subsec. 2.4 of Part I. Then the computer was assigned to do loops on the selected pair of variables with new values. The trend of the correlation is independent of the crystal structure involved.

#### 2.1.1. Correlation between $z_0$ and $\lambda$

The origin of the image plane,  $z_0$ , correlates with the saturation degree,  $\lambda$ , through the elastic potential,  $\text{Re} V(z, z_0, \lambda)$ , of the surface. The integration

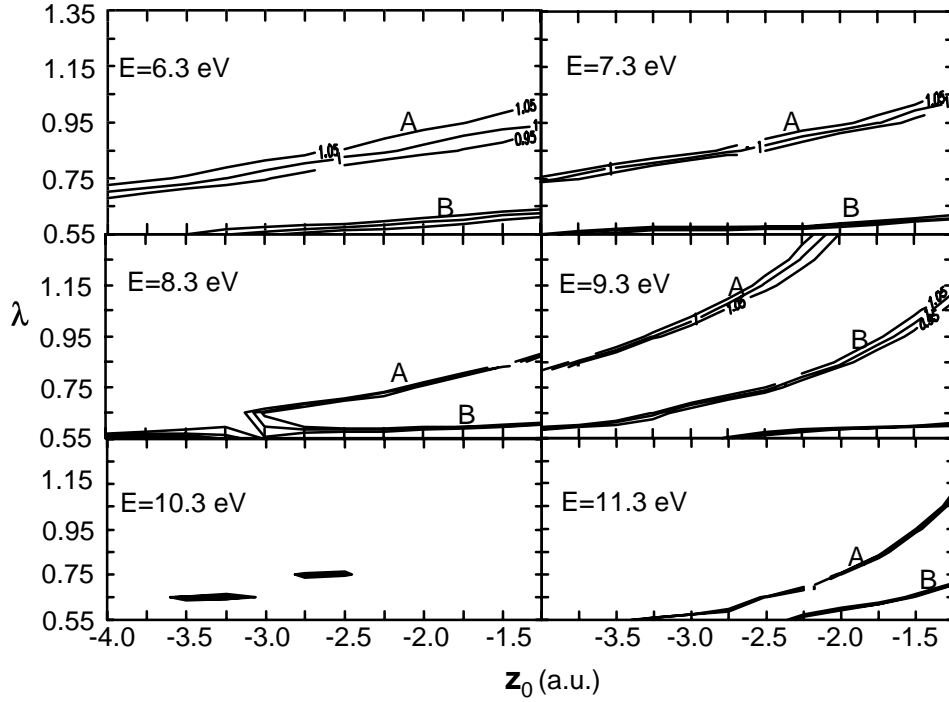


Fig. 1. Correlation between  $z_0$  and  $\lambda$  at different energies.<sup>3</sup> The presence of groups — such as A and B — of infinite solutions for a certain energy and the absence of a universal constant solution for all the energies imply the solution uncertainty due to the independent treatment of the multiple correlated SPB parameters.

of  $\text{Re } V(z, z_0, \lambda)$  determines the phase change of reflected electron beams. Hence, it is essential and realistic to define the  $\lambda(z_0)$  relation in Subsec. 2.4 of Part I to reduce the number of solutions.

Figure 1 shows the correlation between  $z_0$  and  $\lambda$  at various energies. There are groups of correlation curves in each panel corresponding to a  $2n\pi$  phase change of one another. The infinite couples of  $(z_0, \lambda)$  along each curve in a group provide matching between calculated and experimentally detected intensities  $I_c/I_e = 1.00 \pm 0.05$ . In order to find the correlation between the couple of  $z_0$  and  $\lambda$  parameters, it is necessary to collect data  $[(z_0, \lambda)_i, i = 1, 2, \dots, 30]$  from each  $z_0$ - $\lambda$  curve and then integrate  $\text{Re } V(z, z_0, \lambda)$ . The integration ranges from the second atomic plane ( $D_{12}$ ) to infinitely far away (in practice the upper limit is chosen as  $-100$  a.u.) from the surface:

$$I(z_0, \lambda)_i = \int_{D_{12}}^{-\infty} \text{Re } V(z, z_0, \lambda)_i dz$$

$$(i = 1, 2, \dots, N).$$

$N = 30$  is sufficient for statistical analysis. The average of the integration values of each curve in Fig. 1

is

$$I = \frac{1}{N} \sum_{i=1}^N I(z_0, \lambda)_i \quad (N = 30),$$

and the standard deviation is

$$D = \sqrt{\frac{\sum_{i=1}^N (I_i - I)^2}{N(N-1)}}.$$

Table 1 summarizes the integration of  $\text{Re } V(z, z_0, \lambda)$  along the  $z_0$ - $\lambda$  curves. Except for  $E = 10.3$  eV (the boundary of the first Brillouin zone), all the energies present at least two groups of curves that give a solution of  $I_c/I_e = 1.00 \pm 0.05$ . However, there is not a common value suitable for the integrations at all the considered energies. The absence of such an identical integration for all the energies means that no constant  $z_0$  or  $\lambda$  is available for the entire specific spectrum. Therefore,  $z_0$  and  $\lambda$  vary from site to site at the surface. It is further justified that it is essentially reasonable to define the  $z_0(E)$  relation as given in subsec. 2.4 of Part I.

Table 1. Integration of  $\text{Re}V(z, z_0, \lambda)$  along the correlation curves as typically shown in Fig. 1.\*

$(E =)$	Integration of $\text{Re}V(z)$	Deviation	$D/I$
6.3-A	7.8032	0.0648	0.0083
7.3-A	8.0070	0.0631	0.0079
8.3-A	7.3052	0.0243	0.0033
9.3-A	8.5842	0.0131	0.0015
11.3-A	7.1091	0.0016	0.0002
6.3-B	6.6424	0.0453	0.0068
7.3-B	6.6531	0.0660	0.0099
8.3-B	6.7318	0.0742	0.0110
9.3-B	7.6051	0.0273	0.0036

\*Integration ranges from  $D_{12}$  ( $\sim 3.5$  a.u.) to  $-100$  (a.u.).

### 2.1.2. Correlation between $z_1$ and $\alpha$

The spatial integration of the inelastic potential,  $\text{Im}V(z, E)$ , determines the amplitude loss of the electron beams.  $z_1$  and  $\alpha$  are also correlated.

Figure 2 shows the  $z_1$ - $\alpha$  contour plots at different energies. Unlike the couple of  $z_0$  and  $\lambda$ ,  $z_1$  correlates with  $\alpha$  uniquely through one curve at each energy. The trends of  $z_1$ - $\alpha$  change are quite different from those of the  $z_0$ - $\lambda$  plots at various energies. The trends of  $z_1$ - $\alpha$  correlation indicate that the spatial decay of the inelastic damping is rather local at the surface, and varies from site to site and from energy to energy. If one parameter such as  $z_1$  is fixed, then  $\alpha$  will be certain. The correlation further provides the experimental basis for the functionalization of the nonuniform SPB approximation, as given in subsec. 2.4 of Part I.

### 2.1.3. Solution certainty

Generally, correlation between any pair of the SPB parameters, or even the atomic positions,<sup>4</sup> can be obtained by treating them independently. The correlation leads to the uncertainty of solutions at certain energies, as demonstrated. As can be seen from the  $z_0$ - $\lambda$  counter plot of Fig. 1, for example, at 9.3 eV  $\text{Re}V(z)$  desaturates ( $\lambda$  decreases with the outward

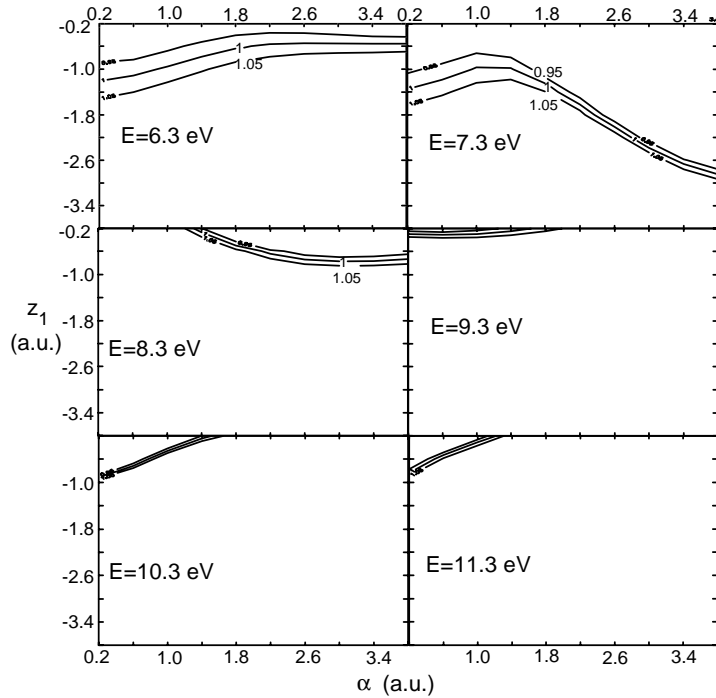


Fig. 2. Scanning contour plots for the correlation between the  $z_1$  and  $\alpha$  parameters at different energies.<sup>3</sup> Different trends of the single (rather than groups as in Fig. 1) correlation curve ( $I_c/I_e \approx 1$ ) at each energy value indicate the nonuniform spatial decay of the inelastic damping. At energies of 10.3 and 11.3 eV,  $\text{Im}V(z)$  saturates ( $\alpha$  increases) with the inward shift of  $z_1$ ; at 9.3 eV,  $\alpha$  is smaller than 1.8 and  $z_1$  is limited to  $-0.4$  a.u.

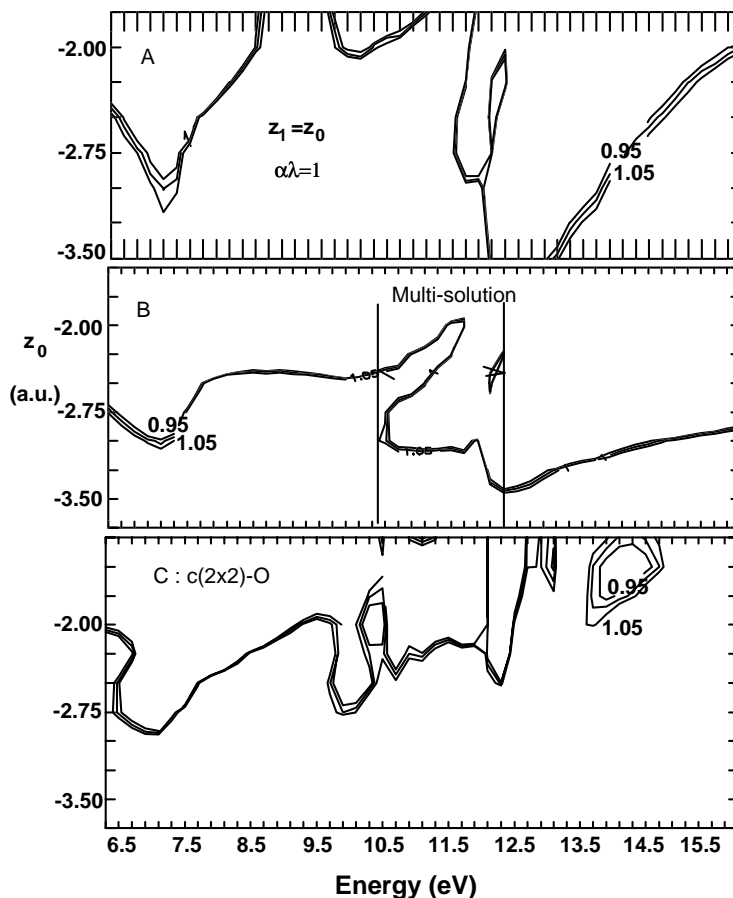


Fig. 3. The uniqueness of the solution obtained with new models and the decoding method for the spectrum collected at  $43.5^\circ$  azimuth.<sup>3</sup> A is compared with B using the same structure but different SPB; B is compared with C using the same SPB but different structure, as indicated. B is preferred due to the unique solution, which justifies the validity of the current-model approximation and the solution certainty.

shift of the image plane,  $z_0$ , from the surface, giving an infinite number of solutions). If one defines a function of  $\lambda(z_0)$  that is orthogonal to the three  $z_0$ - $\lambda$  correlation curves, the three groups of infinite solutions will then be reduced to three finite ones. If one treats all the SPB variables as functions of  $z_0$ , the uniqueness will be realized. Hence, it is justified to limit all the SPB parameters as functions of one variable — the characteristic position of the electron distribution,  $z_0(E)$ .

Figure 3 shows the  $z_0$ -scanning solutions for different barrier and structural models. Plots A and B are the results of identical structural parameters (current model; see Subsec. 3.3 of Part I) but different SPB functions. As denoted, B is the standard case while A has  $z_1 = z_0$  and  $\alpha\lambda = 1$ . This means that the spatial decay of damping is iden-

tical to the Fermi part of  $\text{Re}V(z)$ . C is the result of the same SPB functions as B but includes a structure of  $c(2 \times 2)$  with oxygen being situated  $0.85 \text{ \AA}$  above the unreconstructed lattice plane. The existence of this phase has already been excluded for the O-Cu(001) system.<sup>5,6</sup> Except for the region between 10.5 and 12.3 eV, a unique solution is assured with the single-variable parametrized SPB. Obviously, plot A presents steeply varied dips with too large  $\Delta z_0$  while plot C has no unique solution above 9.5 eV. Plot B, a yield of the solidification of the current bond and nonuniform SPB models and the decoding skills, is preferable to others. Therefore, the approaches in this work are realistic and correct for the particular O-Cu(001) surface. As demonstrated, the approaches have so far enabled VLEED to provide simultaneously integrated

Table 2. Correlation between the bond geometry and the atomic shift in the pairing  $\text{Cu}_3\text{O}_2$  tetrahedron on the  $\text{Cu}(001)\text{-O}$  surface.<sup>7</sup>

Labels (Fig. 5)	Bond geometry (in Å and °)				Atomic shift (Å)				
	BA12	$DCu_x$	$D$	$Q_2$	$D_{12}$	$DO_x$	$DO_z$	$DCu_x$	$DCu_z$
(a)-C	101.0	0.25	$D_{av}$	0.04	1.9086	-0.1852	0.1442	0.25	-0.1635
*a	102.0	0.25			1.9343	-0.1877	0.1682		-0.1495
*b	101.5	0.225			1.9251	-0.1863	0.1553	0.225	-0.1375
(a)-B	104.5	0.25			1.9968	-0.1956	0.2316		-0.1156
(a)-A	107.0	0.25			2.0567	-0.2055	0.2926		-0.0834
(b)-A	102.0	0.25	$D_{av}$	0.03	1.9545	-0.1879	0.1699	0.25	-0.1385
(b)-B				0.05	1.9141	-0.1876	0.1666		-0.1605
(b)-C				0.08	1.8531	-0.1870	0.1614		-0.1939
(c)-A	102.0	0.15	$D_{av}$	0.04	1.9343	-0.1877	0.1682	0.15	-0.0709
(c)-B		0.30						0.30	-0.1859
(c)-C		0.40						0.40	-0.2535
(d)-A	102.0	0.25	$D_1$	0.04	1.9343	-0.1877	0.1682	0.25	-0.0920
(d)-B			$D_2$						-0.2046

\*a and b indicate optimal parameters for the reference (broken lines) spectra in Figs. 5 and 6. Parameter transformation is referred to in Subsec. 2.2 of Part I.

information about the bond geometry, surface topography and the DOS in the valence band.

## 2.2. Capacity and reliability of VLEED

### 2.2.1. Decoding procedures

Calculations were performed with the  $\text{Cu}_3\text{O}_2$  pairing tetrahedron structure illustrated in the Appendix for Fig. 6 of Part I. The variables required in calculations are converted from the bond geometry (see Subsec. 2.2 of Part I. As can be seen from Table 2, any variation of the bond geometry results in a collective dislocation of the surface atoms.

First, all the parameters and constants were set at values optimized in Subsec. 3.3 of Part I. As references for the sensitivity examination, two  $I\text{-}E$  curves were simulated with the  $z_0$ -optimizing method. The optimal structure parameters are shown in Table 2, indicated by \*a and \*b. The corresponding  $z_0(E)$  profiles are given in Fig. 4. Duplications of the corresponding spectra are shown by broken curves in Figs. 5–7.

VLEED spectral sensitivity was examined by letting the code read the initial optimal data in Table 2 (denoted as \*a and \*b) and the  $z_0(E)$

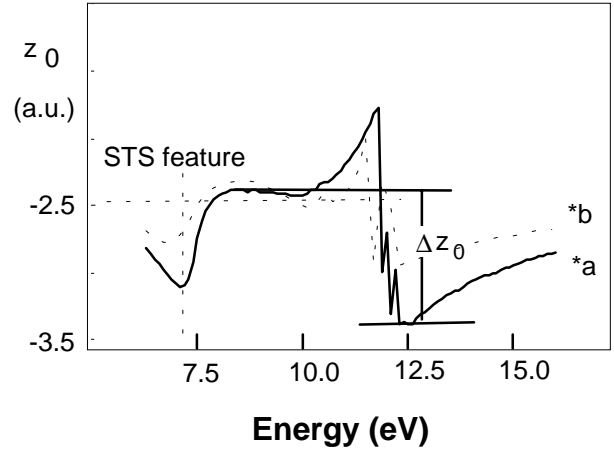


Fig. 4. The optimal  $z_0(E)$  profiles obtained in the original calculations. These curves were read as input iteration by the codes to conduct the sensitivity examination. Spectrum a corresponds to the surface that is more fully developed than spectrum b.

profiles in Fig. 4, and then repeat the calculation by adjusting the individual parameters concerned.

### 2.2.2. Sensitivity to the bond geometry

Figure 5 shows the calculation results obtained by varying the bond geometry. Besides the two bond

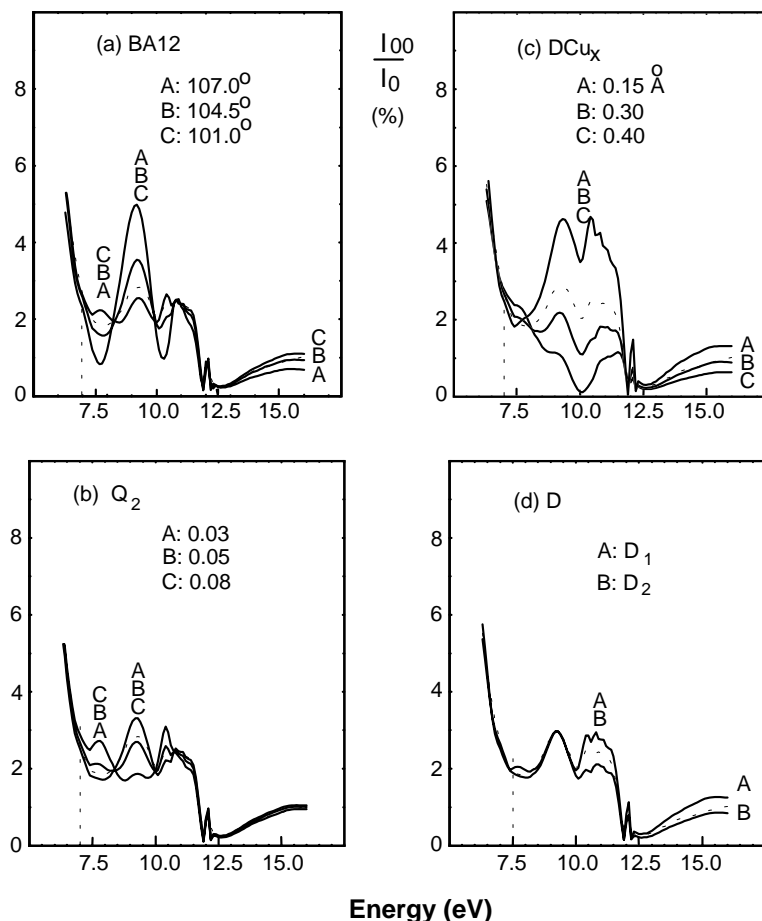


Fig. 5. VLEED spectral sensitivity to the bond geometry.<sup>7</sup> Corresponding variations of parameters are listed in Table 2. Dotted lines are the reference spectrum simulated initially. BA12 and  $Q_2$  modulate the spectral features from 7.0 to 11.0 eV.  $DCu_x$  modulates the intensity between 7.5 and 12.0 eV.  $DCu_z$  has very little effect on the spectrum between 10.0 and 12.0 eV, producing no match to the measured profiles. The bond geometry or crystallography has little effect on features below 7.0 eV.

parameters, BA12 and  $DCu_x$ ,  $Q_2$  was treated as an additional variable. For comparison the effect of individual atomic displacement,  $DCu_z$ , was also considered. The structural sensitivity examination results in Fig. 5 reveal that:

- Adjusting the bond angle BA12 and the bond contraction factor  $Q_2$  modulates the fine-structure features between 7.0 and 11.0 eV, which produces the trends of the measurements at lower oxygen exposures (25–200 L).
- Increasing  $DCu_x$  attenuates the general intensity at energies below the second band gap (< 12.0 eV). This trend agrees remarkably with the spectral features at higher oxygen exposures (> 200 L) and long term aging (> 30 min).<sup>8</sup>

- Changing  $DCu_z$  causes nothing more than a slight change in intensity between 9.5 and 11.5 eV. This provides evidence that the single atomic shift is less realistic than the bond geometry in reaction because no such features had been observed in the measurements.<sup>8</sup>
- Geometry-sensitivity examination indicates that the reaction processes are dominated by the formation of the Cu<sub>2</sub>O bond while the SPB, as a consequence of bonding, varies insignificantly with the small change in bond geometry.

### 2.2.3. Sensitivity to the SPB

Instead of the three constants ( $V_0$ ,  $\delta$ ,  $\gamma$ ) and one variable ( $z_0$ ) in the current modeling approach, eight

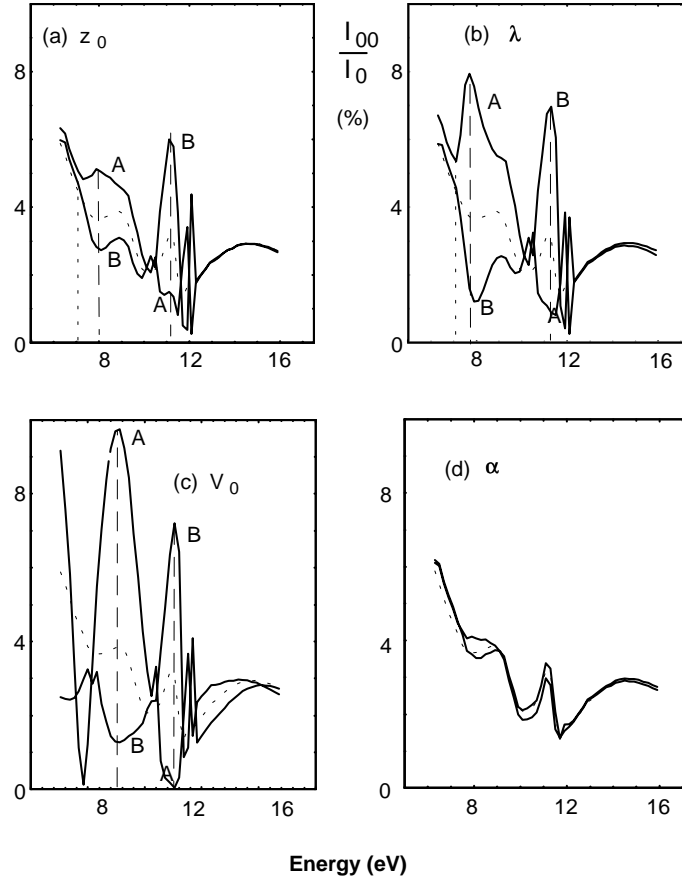


Fig. 6. VLEED spectral sensitivity to the SPB parameters that vary by  $\pm 10\%$ .<sup>7</sup> Panels (a)–(c) show the results of the elastic potential, which leads to the phase change of the diffracted beams. The broken line is the reference spectrum. A 20% change of the  $V_0$ ,  $z_0$  and  $\lambda$  in  $\text{Re} V(z)$  has the similar effect that causes an opposite phase change as indicated. Obviously, the elastic potential dominates the shape of the spectrum at energy below 12.0 eV.

independent SPB parameters were used, as is the convention, to examine the spectral sensitivity to the SPB. The  $\delta$  [in  $\text{Im} V(E)$ ] was not considered as it determines the slope of  $\text{Im} V(E)$  and its value depends on the calibration of the spectral intensity. The corresponding variations of the SPB parameters in Figs. 6 and 7 are varied by 10% rather than simply by adding or subtracting a random amount. This is because most of the parameters, such as  $\lambda$ ,  $z_1$  and  $\alpha$ , are no constants and thus it would be better to change them in an equal percentage for comparison.  $\beta$  and  $\eta$  are introduced as such to modulate the spatial decay of damping at different regions (Subsec. 2.4, Part I):

$$\text{Im} V(z, E) = \begin{cases} \beta \times \text{Im} V(E, z), & z \leq z_1, \\ \eta \times \text{Im} V(E, z), & z_1 < z \leq z_{SL}, \\ \text{Im} V(E, z), & z_{SL} < z, \end{cases}$$

where  $z_{SL}$  is the position of the second atomic plane. The  $z$  axis is directed into the crystal.

Figures 6 and 7 show the spectral sensitivity to the parameters involved in the  $\text{Re} V(z)$  and  $\text{Im} V(z)$ . From the variations of the spectra, it is easy to derive the following:

- The elastic potential  $\text{Re} V(z, z_0, \lambda, V_0)$  dominates the shape of the fine structures. It is true that the integration of  $\text{Re} V(z, z_0, \lambda, V_0)$  makes more sense than the individual limit in determining the phase change of the diffracted beam. Thus, the  $\lambda(z_0)$  parametrization is further justified being essential. It is interesting that a 20% change in these parameters leads to a phase change of  $\pi$ , which is identified as the transition of the spectrum from maximum to minimum at the same energy as indicated in Figs. 6(a)–6(c).

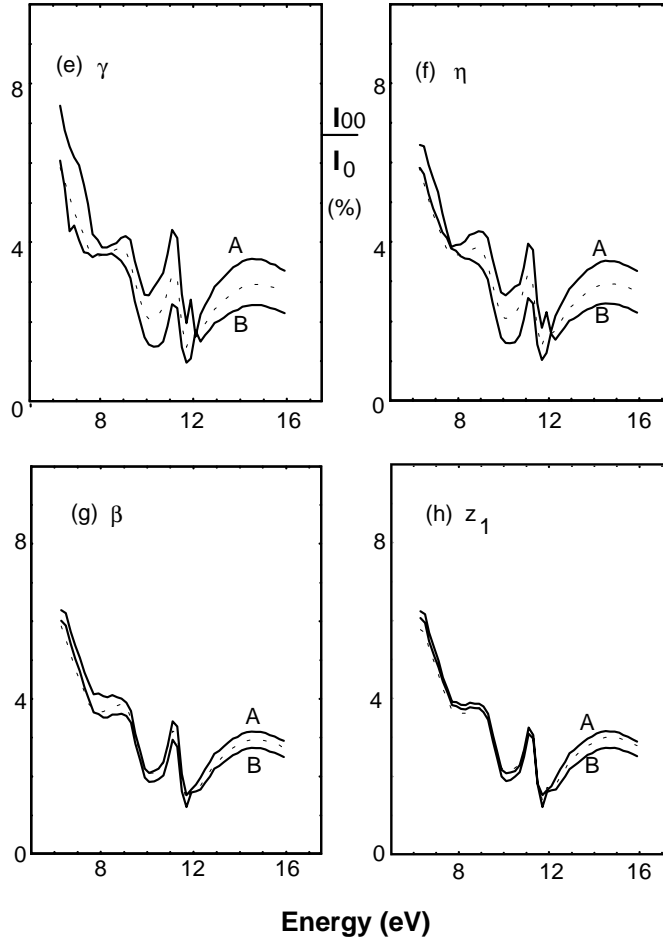


Fig. 7. Panels (d)–(h) are results from varying the parameters in the inelastic potential that dominates the absolute intensity. The similar quantitative effect of  $\gamma$  and  $\eta$  on the intensity indicates that the topmost layer ( $z \leq z_{SL}$ ) dominates the damping. Electrons from below the substrate second plane give no contribution to the damping, proving that the VLEED collects information from a single surface atomic layer.

- The shape of the fine structures is not sensitive to the inelastic damping,  $\text{Im} V(z)$ . All the parameters in the inelastic damping, however, affect the absolute reflectivity of the spectrum. Therefore, all the  $\text{Im} V(z)$  parameters can be functionally dependent on the characteristic variable. The inelastic potential parameters could be used conveniently to compensate for the accuracy in calibrating the measured data.
- By comparing the spectral intensity modulated by  $\gamma$  ( $z \geq 0$ ) with the resultant of  $\eta$  and  $\beta$ , one can find easily that the topmost layer ( $z > z_{SL}$ ) dominates the damping. The resultant of  $\beta(z \leq z_1)$  and  $\eta(z_1 < z \leq z_{SL})$  has the same quantitative effect as  $\gamma$  on the reflectivity. So electrons below

the second atomic plane do not come into play in the VLEED spectra.

- The spectrum is not, however, very sensitive to the variations of  $\alpha$ ,  $\beta$  and  $z_1$ . Thus, approaches in the functional dependence of the insensitive parameters on the characteristic one are substantially necessary. Although the effect of changing parameter  $\delta$  (slope) in  $\text{Im} V(E)$  was not considered, one may use it to compensate for the assumption in data acquisition that the incident current is constant during the increase in the incident-beam energy.
- It is noticed that only the inelastic damping modulates the spectral intensity at energies higher than the second band gap ( $> 12.0$  eV). This fact suggests that the electrons in deeper bands are less

affected by the surface bonding, and as a result they affect insignificantly the elastic potential at the surface.

- Another important fact is that the spectral intensity below 7.0 eV is modulated by neither the bond geometry nor the shape of the elastic potential ( $z_0$  and  $\lambda$ ), as indicated in Figs. 5 and 6. The intensity at this region is, however, sensitive to the inner potential  $V_0$  and parameters in the inelastic damping, as will be discussed;  $V_0$  corresponds to the charge quantity at the surface. Therefore, spectral features below 7.0 eV vary with the surface electron density rather than the bond geometry or the barrier shape.

#### 2.2.4. Indication

VLEED spectral sensitivity both to the bond geometry and to the SPB has been examined in detail. The new approaches enable the factors to be classified as being responsible for the shape [ $\text{Re } V(z)$ ], the absolute intensity [ $\text{Im } V(z, E)$ ] and the partial features (bond geometry) of the VLEED  $I-E$  curves. It should be pointed out that the current conclusions could not be drawn from conventional wisdom by treating all the parameters independently. Besides the adequacy of the calculation code, the reliability of VLEED depends largely on the modeling approaches and decoding skills that must represent reasonably well not only the correlation between the crystal geometry and the SPB but also the real process that occurs. Justification for the capacity and reliability of VLEED leads to new knowledge, summarized below:

- The VLEED spectra are much more sensitive to the bond geometry than to the individual atomic dislocations. Individually varying the atomic position is not practical in simulating the process of surface bond forming. Agreement of the trends between the measurements and calculations by adjusting the bond variables prompts further efforts towards quantifying the O–Cu(001) bonding kinetics, which is the subject of Sec. 5.
- The shape of the  $I-E$  curve is sensitive to the elastic potential  $\text{Re } V(z)$  the integration of which determines the phase change of the diffracted electron beams.
- The absolute intensity of the  $I-E$  curve is dominated by the inelastic damping. Thus the

parameters in  $\text{Im } V(z, E)$  can compensate for the inaccuracy of the calibration of experimental data.

- It is revealed that the inelastic damping predominates in the topmost layer in VLEED. Therefore, LEED at very low energies is the unique technique developed so far that collects nondestructive information from a single atomic layer of a surface, and its energy covers the valence band.

The self-consistency between the outcomes and the constraints (the sense of SPB integration; Subsec. 2.4, Part I) on which the SPB is premised proves sufficiently that the decoding technique and the modeling approaches are essentially correct, and therefore the capacity and the reliability of VLEED are in turn fully uncovered.

### 3. Angle-Resolved VLEED

Thus far, the validity of the models and the decoding skills, as well as the capacity and reliability of the VLEED technique, has been completely justified. We now turn to using these approaches to examine the details of oxygen bonding to the Cu(001) surface.

Hitchen, Thurgate and Jennings measured the VLEED reflectance from an O–Cu(001) surface under various experimental conditions.<sup>8,9</sup> These results formed the unique kinetic–VLEED database available to date. It will be shown in this section and further that the VLEED database is of high value not only in revealing the details of O–Cu interaction but also in judging the validity of the approaches. The association of the kinetic–VLEED data and the multiatom VLEED code with the models and the decoding skills has improved substantially our insight into the electronic process of the O–Cu(001)-surface reaction.

It is shown first in this section that constructing Brillouin zones from the critical energies on the angle-resolved VLEED profiles yields information about the valence bands, the effective mass of electrons and the deformation of the unit cells. Decoding the fine-structure features rewards us with details of the bond geometry, the shape of the SPB and the occupied energy states. It is confirmed that the O–Cu bond forming results in the collective dislocation of surface atoms, as well as the formation of Cu missing rows and O–Cu–O chains. The reaction also

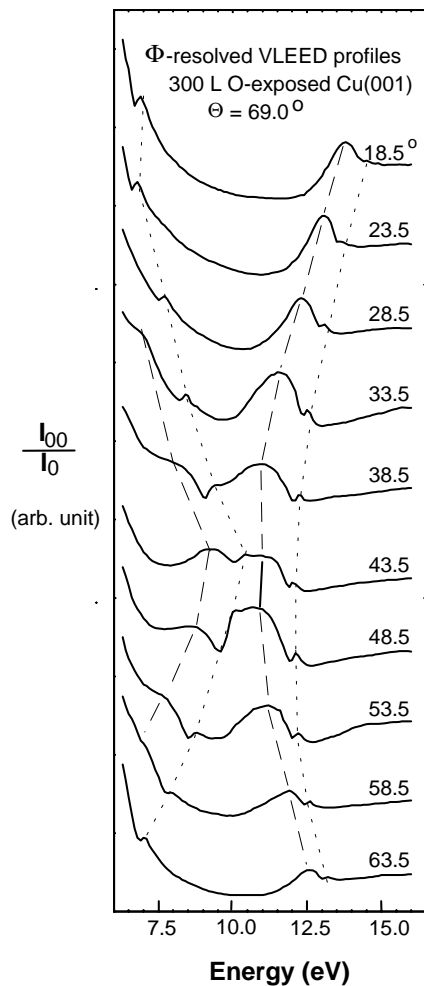


Fig. 8. Angle-resolved VLEED profiles collected from a Cu(001) surface exposed to 300 L oxygen at  $69.0^\circ$  incidence.<sup>9</sup> The azimuth angles are labeled for each curve. There is a “cross-point” at about  $45^\circ$  azimuth. Two small sharp peaks (indicated by dotted lines) appear on each curve. The broadened fine-structure feature (dashed lines) splits when the azimuth moves away from the  $\langle 11 \rangle$  direction.

modifies the valence DOS, the nonuniformity and anisotropy of the SPB, and the reduction both in the work function and in the inner potential constant of the surface.

### 3.1. VLEED profiles

The VLEED (00) beam  $I-E$  profiles to be decoded were collected from a Cu(001) surface exposed to 300 L oxygen.<sup>9,8</sup> For the symmetry consideration, angles from  $18.5^\circ$  to  $63.5^\circ$  with a  $5^\circ$  increment are sufficient to represent the full azimuth of the

surface. The features of the measured VLEED profiles in Fig. 8 can be summarized as follows:

- Two sharp, solitary troughs or violent peaks (indicated by dotted lines) appear on each curve. These two troughs move away from each other as the azimuth moves away from the  $\langle 11 \rangle$  direction. The angle-resolved sharp features divide the VLEED energies (6.0–16.0 eV) into three regions with variation in the energy of the boundaries. Calibration of these critical positions gave a reduction in the work function of  $\sim 1.1$  eV.<sup>10</sup>
- The fine-structure feature (indicated by dashed lines) splits into its separate components as the azimuth moves away from the symmetric point  $45.0^\circ$ . The first component vanishes outside the region of  $33.5^\circ$ – $58.5^\circ$ . The second one becomes narrower while moving away from the symmetric point. Further, the intensity of the second peak tends to be weaker when the azimuth is greater than  $45.0^\circ$ .
- The peak positions and intensities of the curves show a reduction in symmetry relative to the symmetric center. The reduction of the intensities at higher azimuth angles may come from the development of the reaction, as the long-term aging leads to a general attenuation of the spectral intensity.<sup>8</sup> The deviation of the symmetry means that the original  $C_{4v}$  group symmetry has been destroyed upon reaction.

### 3.2. Sharp features: Brillouin zones and energy bands

The primary unit cell in the Cu(001)- $(\sqrt{2} \times 2\sqrt{2})R45^\circ$  structure is the concern of the community of solid-state physicists. As is known,<sup>11,12</sup> the presence of defects and impurities, such as the missing-row vacancy and the oxygen adsorbate, has no effect on constructing either the real lattice or the reciprocal lattice. However, displacements of lattice atoms, such as the  $DCu_x$  for the atoms close to the missing row, or in the  $\langle 11 \rangle$  direction (Fig. 6 of Part I), deform both the real and the reciprocal lattice.

(i) *Brillouin zones and effective masses of electrons.* It was realized<sup>13</sup> that the emergence of a new diffraction beam is independent of the inner potential and the barrier shapes. It depends only on the incident and diffraction conditions, and the two-dimensional geometry of the surface lattice.

Table 3. Positions of the sharp peaks,  $E_{p1}$  and  $E_{p2}$ , in the angle-resolved VLEED profiles of the O–Cu(001) surface. The incident angle is kept constant at  $69.0^\circ$ .

Azimuth	$E_{p1}$ (eV)	$E_{p2}$ (eV)
$18.5^\circ$	5.00	14.50
$23.5^\circ$	5.20	14.00
$28.5^\circ$	5.60	13.30
$33.5^\circ$	8.30	12.50
$38.5^\circ$	9.50	12.20
$43.5^\circ$	10.40	12.00
$48.5^\circ$	10.00	12.20
$53.5^\circ$	8.80	12.30
$58.5^\circ$	5.80	12.60
$63.5^\circ$	5.00	13.20

Emergence happens when the lateral components of the diffracted wave, with vector  $k'_{//}$ , and the incident wave  $k_{//}$  satisfy the Bragg diffraction condition,

$$k'_{//} - k_{//} = g,$$

where  $g$  is the vector of a reciprocal lattice. It is the very Bragg condition that yields the band-gap reflection at the boundary of a Brillouin zone. Therefore, the sharp features closing to the emergence of the new beam on the VLEED spectra arise from the band-gap reflections at the boundaries of Brillouin zones.

Accordingly, two-dimensional Brillouin zones can be constructed from the sharp-peak positions in the angle-resolved VLEED data, as summarized in Table 3. The location of a peak  $E_p$  can be decomposed in  $k$  space as (in atomic units:  $m = e = \hbar = 1$ ; 1 a.u. = 0.529 Å and 27.21 eV)

$$E_p = \frac{k_{\langle 01 \rangle}^2 + k_{\langle 10 \rangle}^2 + k_z^2}{2m^*},$$

with

$$\begin{aligned} k_{\langle 10 \rangle} &= \sqrt{2m^*E_p} \sin \theta \cos \phi, \\ k_{\langle 01 \rangle} &= \sqrt{2m^*E_p} \sin \theta \sin \phi, \end{aligned} \quad (3.2.1)$$

where  $m^*$ , the effective mass of the electron populating near the boundary of the Brillouin zone, is introduced such that it compensates for the reduction of the diffracted  $k'$  due to its energy loss.  $\theta$  represents the incident angle and  $\phi$  the azimuth angle of the incident beam. The resultant wave vectors,  $k_{\langle 10 \rangle}$  and  $k_{\langle 01 \rangle}$ , extend from the center to the

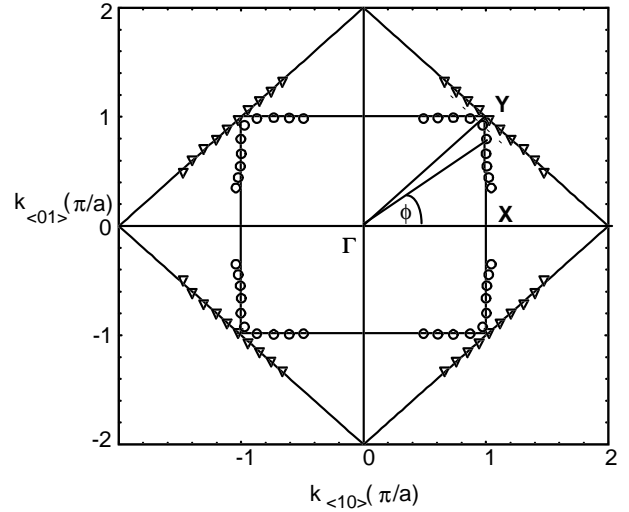


Fig. 9. The first two Brillouin zones (indicated by open circles and triangles) derived from the critical positions on the angle-resolved VLEED profiles, compared with the theoretical ones (solid lines). Matches are achieved by introducing the effective electron masses. Deformation of the first Brillouin zone near the Y point can be related to the  $DCu_x$  in the  $\langle 11 \rangle$  direction of the real lattice.<sup>15</sup>

boundary of the first Brillouin zone. The first two experimental Brillouin zones can then be drawn by optimizing  $m^*$  to match the theoretical calibrations ( $k_{\langle 10 \rangle} = k_{\langle 01 \rangle} = n\pi/a$ ,  $n = 1, 2$ ), as represented by solid lines in Fig. 9. The effective masses of electrons surrounding the Brillouin zone boundaries are optimized with the least-squares method. The optimal values are  $m_1^* = 1.10$  and  $m_2^* = 1.14$ . The increase of  $m^*$  with energy coincides with the trend that the energy loss of the diffracted beam ( $k' = k/\sqrt{m^*}$ ) increases with the incident-beam kinetic energy.<sup>14</sup> On the other hand, the first Brillouin zone contracts at Y but expands near X. The contraction at Y correlates with the atomic shift of  $Cu^{\text{dipole}}$  along the  $\langle 11 \rangle$  direction in the real lattice,  $DCu_x$ , while the expansion near X needs to be identified.

(ii) *In-plane reconstruction.* The mutual-reciprocal relationship between the  $k$ -space with basic vector  $k_i$  and the  $r$  space with basic vector  $a_i$ ,

$$a_i \cdot k_i = 2\pi\delta_{ij}, \quad \delta_{ij} = \begin{cases} 1, & i = j, \\ 0, & i \neq j, \end{cases} \quad (3.2.2)$$

implies that the deviation of the experimental Brillouin zone from the theoretical form originates from

the deformation of the primary unit cell. Therefore, one can trace inversely the  $DCu_x$  from the contraction of the Brillouin zone at  $Y$ .

The distance in  $k$  space,  $\overline{\Gamma Y}$  ( $= \frac{1}{2}|k_i + k_j| = \sqrt{2\pi}/a$ ), correlates with a quantity  $a_{\langle 11 \rangle}$  through the mutual-reciprocal relation (3.2.2):

$$a_{\langle 11 \rangle} \cdot (k_i + k_j) = a_{\langle 11 \rangle} \cdot 2\overline{\Gamma Y} = 2\pi, \quad (3.2.3)$$

which yields

$$a_{\langle 11 \rangle} = \frac{\pi}{\overline{\Gamma Y}} = \frac{a}{\sqrt{2}},$$

corresponding to the shortest row spacing on the (001) surface. Taking the logarithm and derivating from both sides of Eq. (3.2.3), we have

$$\frac{da_{\langle 11 \rangle}}{a_{\langle 11 \rangle}} + \frac{d\overline{\Gamma Y}}{\overline{\Gamma Y}} = 0.$$

Thus, the lateral atomic shift can be expressed as

$$DCu_x = da_{\langle 11 \rangle} = -\frac{a_{\langle 11 \rangle}}{\overline{\Gamma Y}} d\overline{\Gamma Y} = -\frac{a^2}{2\pi} d\overline{\Gamma Y}. \quad (3.2.4)$$

Substituting  $m_1^* = 1.10$ ,  $\theta = 69.0^\circ$  and  $E_{p1} = 10.4$  eV  $= 0.3804$  a.u. (at  $43.5^\circ$  close to the  $\langle 11 \rangle$  direction) into Eq. (3.2.1) yields  $\overline{\Gamma Y}' = \sqrt{2m_1^* E_{p1}} \sin \theta = 0.8104$  (1/a.u.). On the other hand, by adopting  $a = 2.555/0.529 = 4.8308$  (a.u.), one can have the theory value  $\overline{\Gamma Y} = \frac{\sqrt{2\pi}}{a} = 0.9217$  (1/a.u.). Therefore,

$$\begin{aligned} DCu_x &= -\frac{a^2}{2\pi} (\overline{\Gamma Y}' - \overline{\Gamma Y}) \\ &= 0.4133 \text{ a.u.} \\ &\cong 0.22 \text{ \AA}, \end{aligned}$$

which coincides with the values (0.2–0.3 Å) optimized with LEED,<sup>16</sup> XRD<sup>6</sup> and the current VLEED optimization ( $\sim 0.25$  Å). The accuracy of this estimation is subject to the measured peak position  $E_{p1}$ .

(iii) *Valence bands.* As identified, the critical positions correspond to the boundaries of Brillouin zones. It is well known that the boundaries of the Brillouin zones act as edges of the energy bands. Therefore, the zone boundaries divide the current VLEED energies into three regions, as shown in Fig. 10. These regions correspond to the valence bands of copper. Variations of the bandwidth with the azimuth are commonly known in solid-state-physics community.

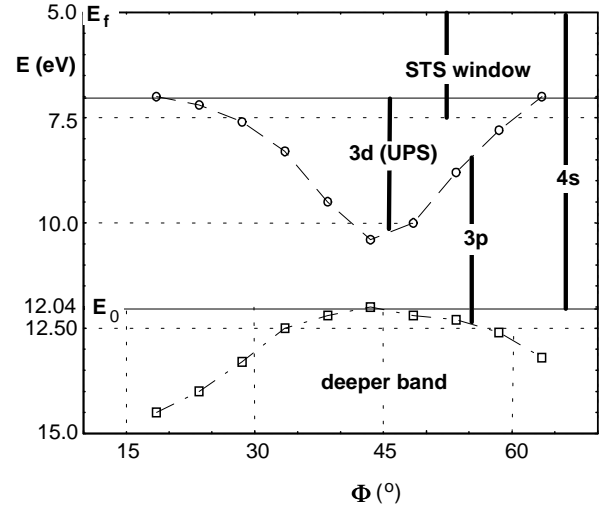


Fig. 10. Band structure extracted from the angle-resolved VLEED profiles.<sup>15</sup> The boundary lines divide the VLEED energies into various bands, as indicated. The current VLEED window covers part of that of STS and UPS.

The first sharp-peak positions varying from 7.0 to 10.4 eV can be ascribed as the bottom of the Cu-3d band, which agrees with the known 3d band structure, 2.0–5.0 eV below  $E_F$  (5.0 eV), as detected by ARUPS.<sup>17,18</sup> Accordingly, the region between the two sharp peaks corresponds to the Cu-3p band. The 3p band overlaps partially the 3d band due to the azimuth effect. The more delocalized 4s band between  $E_F$  and vacuum level  $E_0$  (12.04 eV) fully covers both the 3p and the 3d band. Energies higher than the second Brillouin zone correspond to deeper bands that are not of immediate concern in valence-electron transportation between oxygen and copper.

### 3.3. Fine structures: bond geometry, DOS and 3D SPB

Calculations were conducted by assuming a constant crystal structure during VLEED-data collection. In reality, the aging of the specimen influences slightly the bond geometry and accordingly the spectral intensity. The period of data collection is short enough to allow us to neglect the aging effect during the experiment. The matching between calculated and measured spectra for all the ten azimuth angles has been obtained, but for comparison we just show five replicas in Fig. 11(a). The energy dependence of both the optimized  $z_0(E)$  and the inelastic damping  $\text{Im} V(E, \phi_L)$  are shown in panels (b) and (c). As

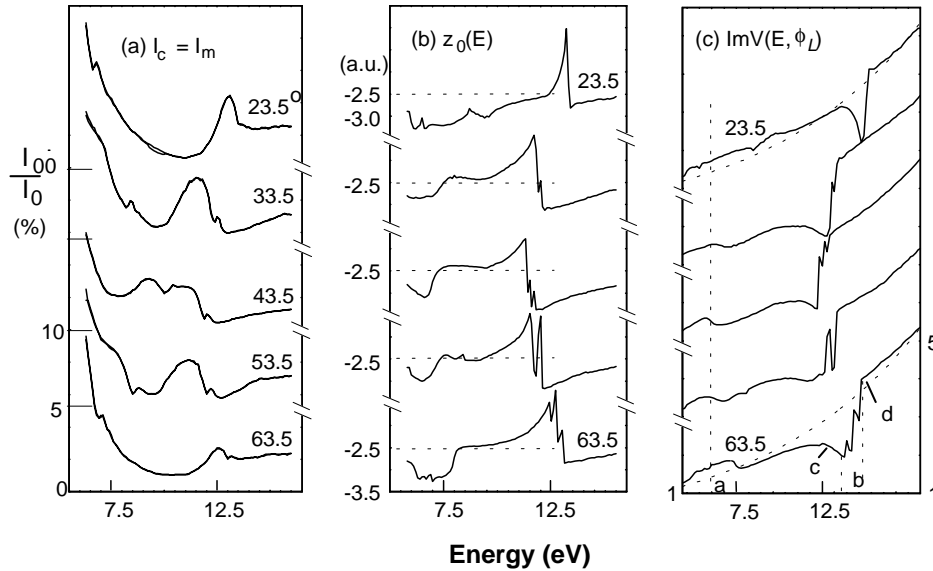


Fig. 11. Besides the bond geometry and the inner-potential constant, outcomes of the  $z_0$ -optimizing calculations contain (a) replications of the measured spectra and (b) the corresponding  $z_0(E)$  profiles.<sup>15</sup> Panel (c) shows damping curves with four significant features. Region a corresponds to hybridized nonbonding states; region b represents band-gap reflection; regions c and d are excitations occurring at edges of different bands. The constant  $z_0$  and monotonic  $\text{Im}V(E)$  for Cu(001) are compared with broken lines.

references, the constant  $z_0$  ( $-2.5$  a.u.) and the monotonic  $\text{Im}V(E, 5.0)$  for the Cu(001) clean surface are compared with dotted lines. Information available from the decoding is summarized in Table 4.

(i) *Bond geometry.* As can be seen, atomic dislocations, layer-spacing relaxation and in-plane reconstruction as well as the adsorbate position are defined uniquely by the bond geometry. The derived atomic arrangement supports the conclusion drawn from the effective-medium-theory calculations by Jacobsen and Nørskov.<sup>19</sup> It was understood that oxygen atoms go underneath the first layer for bonding. Meanwhile, there is a pairing of the Cu dipoles crossing over the missing row. The relaxation is determined by the bond geometry between the adsorbate and the substrate lattices of the first two atomic layers. From the perspective of bond forming, the static atomic position of oxygen should change under various experimental conditions and at different reaction stages; therefore, the discrepancies in atomic positions documented should be no surprise.

(ii) *Joint features of microscopy and spectroscopy.* As mentioned before, the  $z_0(E)$  curves in Fig. 11(b) exhibit joint features of topography and DOS

spectroscopy. It is noticed that the shapes and intensities of the  $z_0(E)$  curves, as well as the damping in Fig. 11(c), vary apparently with the azimuth. At  $43.5^\circ$ , near the  $\langle 11 \rangle$  direction, the  $z_0(E)$  curve provides the maximal  $\Delta z_0 \sim 0.52 \text{ \AA}$  closing to the scale difference of the STM image. This can be a clear indication of the nonuniformity and anisotropy of the SPB, as noted by Baribeau *et al.*<sup>20</sup> in their VLEED simulations. They indicated that the damping is no more isotropic due to oxygen adsorption. It is clear now why we were unable to fit the VLEED spectra near the  $\langle 11 \rangle$  direction without taking the nonuniform and anisotropic SPB into account.

The calculations yield the change in energy states that contribute to the damping. As indicated in Figs. 11(b) and 11(c), there are several notable regions exhibiting DOS features:

- (i) Features below  $7.5$  eV are independent of azimuth angles. These humps coincide with the O-Cu(110) STS and PES signatures around  $7.1$  eV, which have been specified as the contribution of nonbonding states of  $\text{O}^{-2}$ . The antiresonance of this feature (intensity independence of the azimuth and incident energy) on the O-Cu(001) surface

Table 4. Detailed information from the angle-resolved VLEED spectra of the Cu(001)-(2√2 × √2)R45°-2O<sup>-2</sup> surface shows the integrity of the bond model.<sup>15</sup>

Controlling variables	$Q_1, Q_2$	0.12, 0.04
	BA12 (°)	102.0
	DCu <sub>x</sub> (Å)	0.250
Atomic shifts (Å)	DCu <sub>z</sub>	-0.1495
	DO <sub>x</sub>	-0.1876
	DO <sub>z</sub>	0.1682
Relaxation	D <sub>12</sub>	1.9343
Bond length (Å)	BL1	1.628
	BL2	1.776
	BL3(2)	1.926
Bond angle (°)	BA13	105.3
	BA23	99.5
	BA33	139.4
Inner potential	$V_0$ (eV)	10.50
Im $V(E)$	$\gamma$	0.9703
	$\delta$	6.4478
Reduction of work function	$\Delta\phi$ (eV)	1.20
Microscopy features	$\Delta z_{\text{VLEED}}$ (Å)	0.52
$z_0(E)$ spectral features (energy states)	< 7.5 eV	Hybridization
	2nd BZ boundary	Band-gap reflection
	Around BZ boundary	Band-edge excitation
BZs	Fig. 9	
Valence bands	Fig. 10	

has been confirmed with PES by Warren *et al.*,<sup>21</sup> indicating a strong one-dimensional localization of the [O<sup>-2</sup>:Cu<sup>-2</sup>:O<sup>-2</sup>] chain. Coincidence of VLEED (reduction in the work function) with STS (polarization states) in the above- $E_F$  (antibonding) and the below- $E_F$  (nonbonding) features can be convincing evidence that the oxygen adsorbate hybridizes itself and polarizes electrons of its neighboring metal atoms.

- (ii) Band-gap reflection along the boundary of the second Brillouin zone is apparent, while such reflection at the boundary of the first Brillouin zone is invisible near the symmetry point (45°). The invisible features are obviously due to the strong overlap of the

Cu 4s3d3p bands near the  $\langle 11 \rangle$  direction, as illustrated in Fig. 10.

- (iii,iv) The damping surrounding the second Brillouin zone can be featured as electron excitation at the edges of different bands. The excitation of electrons from the bottom of a band seems to be harder than that from the top edge of a band, where the electrons might be denser.

#### 4. Inner Potential and Work Function

The bond-and-band model explains self-consistently the reduction both in the inner-potential constant and in the work function. It is identified that the inner potential relates to the charge quantity and

the work function depends on the density of the polarized electrons at the surface. With expansion of sizes and elevation of energy states, metal dipoles are responsible for the reduction in the local work function. Electron transportation due to reaction dominates the change of the inner-potential constant. Besides, at very low energies, the exchange interaction between the energetic incident beams and the surface is insignificant, and hence VLEED is proven as a technique for nondestructive information from the top layer of a surface.

## 4.1. Findings

### 4.1.1. Beam-energy-reduced $V_0$

The muffin-tin inner-potential constant  $V_0$  is an important parameter required to achieve the best fit between theoretical calculations and the experimental measurements of LEED spectra. Earlier investigations<sup>22</sup> revealed that the  $V_0$  decreases with the energy of the incident beams (the so-called  $E$ -reduced  $V_0$ ); and it was suggested that the  $V_0$  was affected by the surface dipole layer. Investigating the energy dependence of the  $V_0$  of Ni and Cu surfaces, Jennings and Thurgate<sup>22</sup> found that the  $V_0$  decreases exponentially with the increase of the incident energy. This reduction was explained with a free-electron-like scheme where the exchange–correlation interaction between the metal surface and the incident electrons will be weakened as the electron velocity increases. The moving electrons with higher energy reduce the  $V_0$  of the surface. Measurements showed, however, that the  $V_0$  changes insignificantly at energies lower than 40 eV for the Cu surfaces, indicating the insignificance of energy effect on the  $V_0$  at very low energies. Rundgren and Malmstrom<sup>23</sup> suggested that the  $V_0$  decreases as energetic incident beams bombard the surface and drag out the surface ion cores to neutralize the surface negative charges. The sputtering of the surface by the incident beams reduces the quantity of net charges. If one electron is sputtered away from the surface, the residual ion core will also reduce the net negative charge. Therefore, the quantity of surface charges dominates the  $V_0$ .

### 4.1.2. Oxygen-reduced $V_0$

For systems with chemisorbed oxygen, the variation of  $V_0$  appeared to be much more complicated. The

amount of the reduction varies with the crystal structure used in calculation. For a Cu(001)-c(2 × 2)-2O and a (2√2 × √2)R45°-2O structure, the reduction was found to be 1.21 and 2.15 eV, respectively.<sup>24</sup> Calculations of VLEED  $I$ - $E$  curves in the last section with the Cu<sub>3</sub>O<sub>2</sub> bond model require a 1.06 eV (9.2%) reduction in the  $V_0$  from the bulk value of Cu(001), 11.56 eV. A similar conclusion has also been drawn by Pfnür *et al.*,<sup>25</sup> who found in their VLEED calculations that it is necessary to use a step function to describe the reduction in the  $V_0$  of the O–Ru top layer. It is certain that oxygen chemisorption results in a pronounced reduction in the  $V_0$ . With few interpretations, the underlying mechanism of the O-reduced  $V_0$  in VLEED is still ambiguous.

Figure 6(c) compares the effects of varying the  $V_0$  on the calculated VLEED spectrum by using the Cu<sub>3</sub>O<sub>2</sub> model. The solid curve is a duplication of the measurement optimized with  $V_0 = 10.50$  eV. The remaining two curves result from varying the  $V_0$  from 10.50 to 10.50 × (1 ± 10%) eV. It can be seen that the variation of the inner potential from –10% to 10% leads to a phase change of  $\Delta\Phi \cong \pi$ . Evidently, the optimal value of  $V_0 = 10.5$  eV for the best fit is appropriate.

### 4.1.3. Oxygen-reduced-and-localized $\phi_L(E)$

Another striking feature of oxygen chemisorption is the reduction in the work function,  $\phi_L(E)$ . Characterization of the  $\Delta\phi$  has hence been developed as one standard means of determining the surface electronic properties. Hofmann *et al.*<sup>26</sup> and Benndorf *et al.*<sup>27,28</sup> found in their experiments that the  $\phi$  decreases when oxygen is incorporated into the Cu(001) surface. From a HREELS study Dubois<sup>29</sup> concluded that oxygen chemisorbs threefold hollow sites on the Cu(111) surface, either in or below the outmost plane of Cu atoms, resulting in a work-function change. Ertl and Rhodin<sup>30</sup> suggested that the  $\Delta\phi$  is due to the formation of the dipole layer. Lauterbach *et al.*<sup>31</sup> and Rotermund *et al.*<sup>32</sup> attributed the  $\Delta\phi$  to an inverted dipole moment of the oxygen atom when it goes beneath the surface. However, analytical correspondence between the work function and the dipole layer was hard to establish.

## 4.2. Possible mechanisms

As described in Subsec. 2.2 of Part I, c(2 × 2)-2O<sup>–1</sup> domains, or the off-centered CuO<sub>2</sub> pairing pyra-

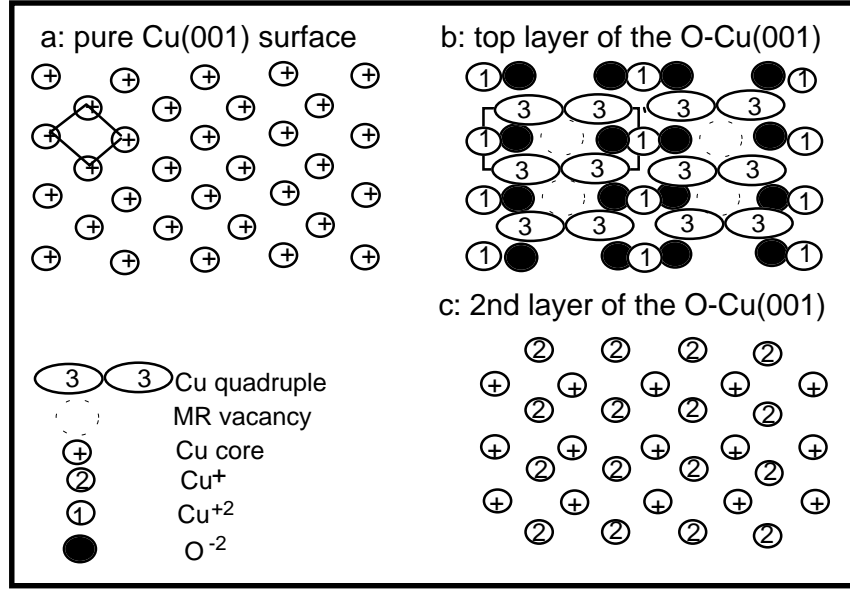


Fig. 12. Surface-charge distribution in both clean and O-chemisorbed Cu(001) surfaces.<sup>34</sup> (a) Pure Cu(001) surface with Cu ion cores regularly arranged in the Fermi sea; (b), (c) the top and the second layer of the Cu(001)- $(2\sqrt{2} \times \sqrt{2})R45^\circ-2O^{-2}$  surface. Panels (a) and (b) match closely the STM images (Fig. 1 of Part I).

mid, evolves into the Cu<sub>3</sub>O<sub>2</sub> pairing tetrahedron that gives rise to the Cu(001)- $(2\sqrt{2} \times \sqrt{2})R45^\circ-2O^{-2}$  phase. Figure 12 illustrates the variation of the surface charge caused by the reaction. Comparing with the clean-Cu(001) surface with ion cores arranged regularly in the Fermi sea, as shown in panel (a), panels (b) and (c) correspond to the top and the second layer of the Cu(001)- $(2\sqrt{2} \times \sqrt{2})R45^\circ-2O^{-2}$  surface. Cu<sub>3</sub>O<sub>2</sub> bonding results in two hybridized-O<sup>-2</sup> ions, one Cu<sup>+2</sup>, two Cu<sup>dipole</sup>, and a missing-row vacancy in a complex unit cell in the top layer. In the second layer, each Cu atom in every other row along the [010] direction contributes one electron to the oxygen atom. Two Cu<sup>+</sup> ions are produced in a unit cell. Panels (a) and (b) illustrate satisfactorily the corresponding STM signatures of Jensen *et al.*<sup>33</sup> In particular, panel (b) can account for the depressions and the “dumbbell” protrusions that bridge over the missing rows.

#### 4.2.1. Oxygen-and-beam-energy-reduced $V_0$

The Cu<sub>3</sub>O<sub>2</sub> model can account for the reduction of  $V_0$  caused by the Cu<sub>3</sub>O<sub>2</sub> bond forming. Initially, there are four Cu atoms in a Cu(001)- $(2\sqrt{2} \times \sqrt{2})R45^\circ-$

$2O^{-2}$  unit cell in the top layer. The chemisorption of O<sub>2</sub> leads to one Cu atom missing. The oxygen atom catches one electron from each of the top and the second substrate layer. The total number of electrons in each layer contributing to the  $V_0$  is reduced by the adsorption of oxygen (with 8 electrons for each O atom) and the removal of Cu (with each Cu atom there are 29 electrons). The transportation of the two electrons from the second layer to the oxygen adsorbate also varies the  $V_0$  of both the top and the second layer. Hence, the relativistic charge quantity in the top layer is

$$\begin{aligned} & \{ [29e \times 2(\text{Cu dipole}) + (29 - 2)e \times 1(\text{Cu}^{+2}) \\ & \quad + 29e \times 0(\text{MR})] \\ & \quad + [(8 + 2)e \times 2(\text{O}^{-2})] \} / [29e \times 4(\text{Cu})] \\ & = 105/116 = 90.5\% \\ & \cong 10.50/11.56 = 90.8\% \text{ (VLEED optimization)}. \end{aligned}$$

In the second layer, each Cu atom in every other row along the [100] direction donates one electron to the oxygen adsorbate. In the case of a Cu atom that has lost one electron, the residual ion core will

also reduce the  $V_0$  due to its residual positive charge. Every loss of an electron equals taking two electrons away from the sum of the negative charge, so that the relativistic variation of the  $V_0$  of the second layer is

$$\begin{aligned} & [29e \times 2(\text{Cu}) + (29 - 1)e \times 2(\text{Cu}^+)] / 29e \times 4(\text{Cu}) \\ & = 114/116 = 98.2\%. \end{aligned}$$

Thus the net charges of the top and the second layer are reduced by 9.5% and 2%, respectively. The net charge finally approaches the bulk value in the third metallic layer or below, the  $V_0$  of which is less affected by the reaction according to the current model. The  $V_0$  gradually approaches the bulk value of the clean Cu(001) when getting inside into the crystal, but the deeper layers are beyond the scope of VLEED (Subsec. 1.2). Agreement between the analysis and the numerical optimization of the  $V_0$  for the top layer further evidences the reality and integrity of the  $\text{Cu}_3\text{O}_2$  bond model for the  $\text{Cu}(001)-(\sqrt{2} \times 2\sqrt{2})\text{R}45^\circ-2\text{O}^{-2}$  surface reaction.

Although the analysis is simply based on a classical viewpoint for the particular  $\text{Cu}(001)-(\sqrt{2} \times \sqrt{2})\text{R}45^\circ-2\text{O}^{-2}$  phase, the result reveals the correlation between the bond forming and the reduction of the  $V_0$  and the work function. It is clear that the  $V_0$  relates to the charge quantity of the corresponding layer, and that at very low energies the exchange interaction between the incident beams and the surface is weak enough to be neglected. The plasma excitation energy is often  $\sim 15$  eV below  $E_F$  and the incident energy is not sufficient to generate plasma at the surface. This adds another advantage to VLEED for nondestructive detection.

#### 4.2.2. *Oxygen-reduced $\phi_L(E)$*

The relation between  $\phi_L(E)$  and  $n(E)$  has been given in Subsec. 2.3 of Part I. As justified, the  $z$ -directional integration of  $\rho(x, y, z)$ , from the second layer to infinitely far away from the surface, yields the local DOS  $n(x, y)$  which contributes to the SPB as well. Since VLEED integrates over large surface areas, all the quantities depending on coordinate  $(x, y)$  become  $E$ -dependent. Therefore, at a certain energy the VLEED integration results  $n(x, y)$  into  $n(E)$

which relates to the occupied DOS and hence the local work function.

It is worth emphasizing that the work function is dimensionless and depends uniquely on the electron density at the surface. However, the concept  $\phi_L$  holds for large surface areas over which VLEED integrates for the DOS, and  $\phi_L$  is also extended to being energy-dependent. As justified, the work function depends uniquely on  $n(E)$ , a  $z$ -dimensional integration of  $\rho(x, y, z)$  at energy  $E$ .  $z_0$  is the boundary of  $\rho(x, y, z)$  [ $\rho(z_0) = 0$ ]. Clearly, the work function is uniquely determined by  $z_0$ . As we found,  $\Delta z_0 \cong 1.0$  a.u. (from  $-2.3$  to  $-3.3$  a.u., close to the gray scale of the STM image) corresponds to a  $\Delta\phi \cong -1.2$  eV reduction. This quantity coincides with the PEEM results of the O-Pt system though the two systems seemed irrelevant. The band model in Subsec. 2.3 of Part I explains that  $\Delta\phi$  originates from the formation of the antibonding dipoles. The antibonding subband is induced by either  $\text{O}^{-1}$  or the nonbonding lone pairs of  $\text{O}^{-2}$ . In real space, the dipoles buckle up with expansion of sizes and elevation of energy states. The buckling dipole changes nothing about the net charge of the surface layer but shifts the critical position  $z_0$  outward from the surface. The SPB is more saturated due to the dipole formation. Therefore, the dipoles have no apparent influence on the  $V_0$  but occupy the empty DOS above  $E_F$ . Because VLEED integrates over a large area of the surface, it is impractical to try to discriminate the  $V_0$  from site to site on the surface.

In summary, the analytic correspondence has been established to quantify the behavior of surface electrons. It is clear now that the oxygen-reduced  $V_0$  and work function originates from the surface bonding. The  $V_0$  relates to the quantity of net charges while the  $\phi$  depends on the  $z$ -dimensional distribution of polarized electrons. It is clarified that the buckling dipoles reduce the  $\phi$  by increasing the occupied DOS at the surface while the dipoles affect little the  $V_0$ . It is also justified that at very low energies the exchange interaction between the incident beams and the surface is too weak to affect either the quantity or the distribution of the surface charges. Therefore, VLEED is an ideal means of collecting nondestructive information about the behavior of surface electrons.

## 5. Exposure-Resolved VLEED

The most striking aspect of oxygen-chemisorption study is the kinetics of bond formation. As the bottleneck, the bonding kinetics has challenged every effort over the past few decades. Little had been known quantitatively until the exercise reported in 1997,<sup>35</sup> though the sequential phases had been confirmed by STM<sup>33</sup> and XRD<sup>6</sup> about the O-Cu(001) bonding kinetics. This section will show the quantification and the corresponding insight into the bonding kinetics and the process of electronic transportation of the O-Cu(001) surface.

### 5.1. VLEED data: four-stage reaction kinetics

Figures 13(a)–13(c) show the exposure-resolved VLEED (00) beam reflectance  $I_{00}/I_0$  versus the incident beam energy measured at 70° incidence and 42° azimuth.<sup>8</sup> It is obvious that the fine-structure features are very sensitive to the oxygen exposure. Typical variations are represented by the peaks, as indicated by the dotted lines in Figs. 13(a)–13(c), at 7.1, 9.1 and 10.3 eV. These peaks show that the reaction progresses in four discrete stages:

- (i)  $\Theta_O \leq 30$  L: The peak at 7.1 eV decreases in magnitudes until the oxygen exposure reaches 30 L, while other peaks show little change.
- (ii)  $30 \text{ L} > \Theta_O \leq 35$  L: The decreased peak intensity at 7.1 eV recovers a little.
- (iii)  $35 \text{ L} > \Theta_O \leq 200$  L: The first peak attenuates while one new peak at 9.1 eV emerges; and then both the peak at 9.1 eV and the peak at 10.3 eV have an increasing maximum of up to 200 L.
- (iv)  $\Theta_O > 200$  L: When the exposures are greater than 200 L, a general attenuation of the entire spectrum occurs.

Besides, the peak at 10.3 eV moves towards lower energy with increasing oxygen exposure. This peak shift corresponds to the increase of  $DCu_x$ , as quantified in Subsec. 3.2.

### 5.2. Geometrical sensitivity

The calculation procedures are the same as those used in Sec. 3. In calculation, the bond parameters and the  $z_0(E)$  curve for the 400 L oxygen-exposure data are optimized first. The optimal parameters

are  $Q_2 = 0.04$ ,  $BA12 = 102.0^\circ$ ,  $DCu_x = 0.25 \text{ \AA}$ , as listed in Table 5. The optimal  $z_0(E)$  curve for 400 L is indicated in Figs. 13(d)–13(f). Regardless of the accuracy of the single-variable parametrization and the extent to which the SPB varies with oxygen exposure, we then examined the structural sensitivity of the 400 L spectrum. Geometrical examination was conducted by adjusting one geometrical parameter at a time and keeping the others and the  $z_0(E)$  curve undisturbed.

Figures 13(d)–13(f) compare the calculation results of individually varying the three bond variables BA12,  $Q_2$  and BL2, and the displacement  $DCu_x$ . The results show the following trends:

- Simulation of the entire set of the exposure-resolved VLEED data can be made by keeping the oxygen coverage constant at 0.5 monolayer. This implies that the extra oxygen atoms due to increasing exposure promote the reaction. The additional oxygen does not participate directly in the reaction after the saturation of adsorption. The promotion may be treated as postsaturation effect. So, no quantitative correspondence between exposure (measured in langmuirs —  $10^{-6} \text{ s} \cdot \text{torr}$ ) and coverage (measured in monolayers, ML) can be established, as justified in many earlier studies.<sup>36</sup> Further evidence of the postsaturation effect is that the relaxation of the layer spacing increases with oxygen exposure. However, it is still a puzzle as to how the extra oxygen adsorbate could enhance the surface reaction without direct involvement.
- The results of the geometrical-sensitivity examination, especially panels (e) and (f), *incredibly* coincide with the trends in the measurements of panels (b) and (c), respectively. This fact indicates that the process of the Cu<sub>2</sub>O bond forming dominates the spectral features while the SPB change is insignificantly sensitive to the oxygen exposures. It is therefore further proved that the bond variables are more realistic than the displacements of rigid spheres and that the corresponding parametrization of the SPB is essentially correct.
- The four discrete reaction stages can be simply expressed in terms of a corresponding variation of the bond variables. For instances, features appearing in the range of 35–200 L are dominated by the increase of  $\angle 102$ , while features for the exposure greater than 200 L are dominated by  $DCu_x$  alone.

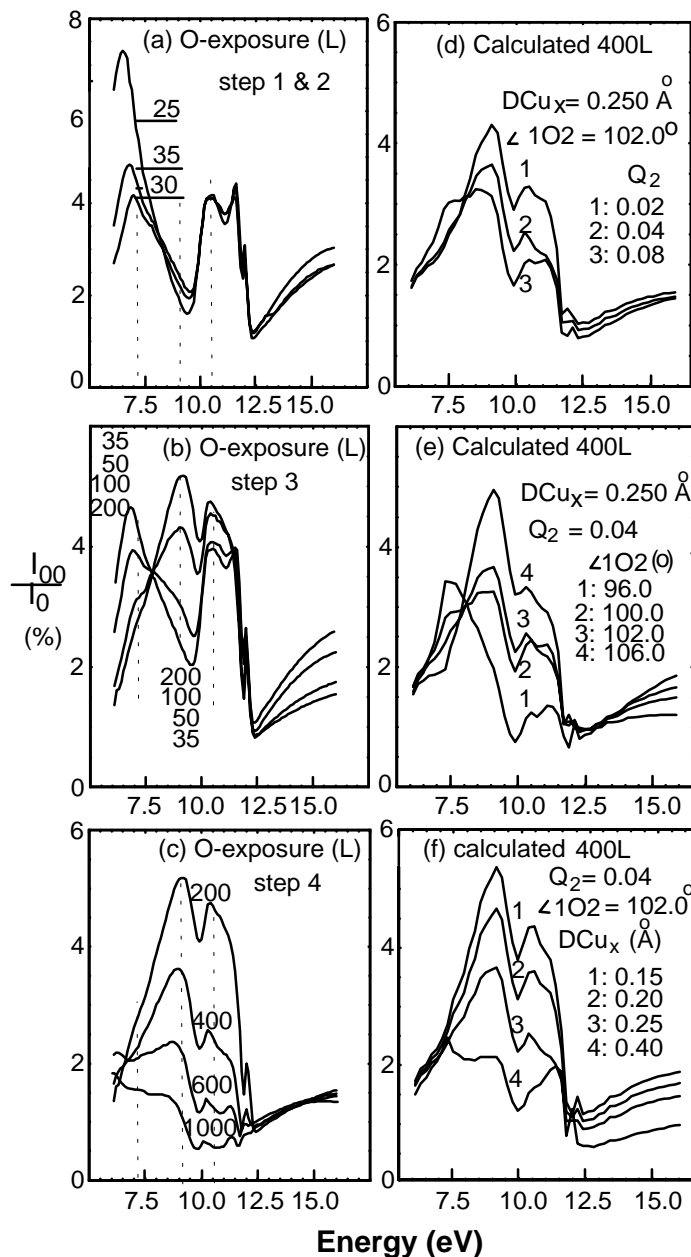


Fig. 13. Exposure-resolved VLEED spectra (a)–(c) measured at  $70.0^\circ$  incidence and  $42.0^\circ$  azimuth from the O–Cu(001) surface,<sup>8</sup> and the calculated results (d)–(f) from varying individual bond variables.<sup>35</sup> Variations of intensities in panels (a)–(c) at 7.1, 9.1 and 10.3 eV show four reaction stages. Calculation results (d)–(f) from varying bond variables  $Q_2$ ,  $\angle 1O2$  and  $DCu_x$  for 400 L oxygen exposure provide the resemblance of the measurements at different stages.

From 30 to 35 L, the recovery of the peak at 7.1 eV can be realized by increasing  $Q_2$  with smaller  $\angle 1O2$  and smaller  $DCu_x$ .

- Calculation by varying  $DCu_z$  was also carried out to examine the effect of individual atomic shifts. The result is the same as in Subsec. 2.2. Variation of  $DCu_z$  gives a little change of the spectral

intensity between 9.5 eV and 11.5 eV, indicating that the individual atomic shift is not realistic for describing the kinetics of reaction.

It is feasible to find optimal bond parameters from the 400 L result for different oxygen exposures. By assuming that  $z_0(E)$  is insensitive to the

Table 5. Four-stage O-Cu(001)-surface bonding kinetics.<sup>35\*</sup>

Reaction stages		1 (< 30 L: BL1 formation); 2 (30–35 L: BL2 & ∠1O2 change); 3 (35–200 L: ∠1O2 expansion) 4 (> 200 L: DCu <sub>x</sub> increase)								
Exposure	(L)	25	30	35	50	100	200	<u>400</u>	600	≥ 800
Bond geometry	$Q_2$	0	0	0.04	0.04					
	BA12	92.5	94.0	98.0	100.0	101.0	102.0			
$Q_1 = 0.12$	$DCu_x$	0.125	0.150	0.150	0.150	0.150	0.150	0.250	0.355	0.450
Atomic shift (Å)	$-DCu_z$	0.1460	0.1440	0.1268	0.0938	0.0844	0.0709	0.1495	0.2239	0.2849
	$-DO_x$	0.1814	0.1796	0.1802	0.1831	0.1852	0.1877			
	$DO_z$	-0.0889	-0.0447	0.0618	0.1158	0.1422	0.1682			
	$D_{12}$	1.7522	1.7966	1.8287	1.8824	1.9086	1.9343			
Bond length (Å)	BL1	1.628								
	BL2	1.850		1.776						
	BL3	1.8172	1.8326	1.8833	1.8983	1.9053	1.9121	1.9262	1.9396	1.9505
Bond angle (°)	BA13	95.70	98.82	104.24	105.12	105.64	105.33	105.30	104.01	103.83
	BA23	91.80	93.11	95.75	96.46	96.83	95.18	99.52	101.67	103.43
	BA33	165.87	160.83	145.26	144.32	143.02	141.82	139.43	135.38	135.71

\*An empty space is identical in value to that in the previous cell. All information is provided by the controlling variables (BA12,  $Q_2$ ,  $DCu_x$ ). Error bars for bond variables are 0.010 Å and 0.2°. The SPB constants are  $V_0 = 10.50$  eV,  $\gamma = -0.9703$ ,  $\delta = 6.4478$ .

exposures, we repeated calculations to match the intensities of the three peaks of all the measurements in Figs. 13(a)–13(c). The calculations were performed with a careful search over a large range and smaller steps of the variables. The optimal structural parameters for various exposures are given in Table 5.

### 5.3. Cu<sub>3</sub>O<sub>2</sub> bonding and band-forming kinetics

In order to test in detail the extent to which the SPB varies during the increase of oxygen exposure and hence to confirm the assumption that the SPB is relatively insensitive, the VLEED calculations at other exposures with the optimal geometry values in Table 5 were repeated, but this time  $z_0(E)$  was allowed to vary until a duplication [ $I_c(E)/I_e(E) = 1.00 \pm 0.01$ ] of the experimental data was obtained.

Figure 14 shows the offset  $z_0(E)$  profiles that produce the  $\text{Im} V(E, \phi_L)$  curves and duplicate the measured spectra in Figs. 13(a)–13(c). It is seen that the  $z_0(E)$  curves, in general, are insignificantly sensitive to the oxygen exposure. They are similar in shape except for minimal variations below 7.5 eV at 25 L

exposure. This is further evidence of the assumption that the VLEED reflectance is much less sensitive to the SPB than to the bond geometry during the increase of exposure. The slight outward shift ( $-z$  direction, relative to  $-2.5$  a.u., as indicated by the broken lines) of the  $z_0(E)$  curves at higher exposures increases  $n(E)$ ; and, as a result, the increase of the  $n(E)$  reduces the work function.  $z_0(E)$  is the contribution of the occupied DOS,  $n(E)$ , which is convoluted by real space [local spatial DOS  $n(x, y)$ ] due to multiple diffraction, but the convolution is minimally important in the VLEED regime. The nonconstant form of  $z_0(E)$  can be understood as being due to the O-induced “rather local” properties as revealed by STM, and the variation in the DOS as being due to electron transportation. The localization originates from the vacating, ionizing and polarizing of the surface atoms. The variation of DOS is due to the electronic process discussed in Subsec. 2.2 of Part I.  $\Delta z_0(E)$  in the  $z$  direction is about [ $-2.3$ –( $-3.3$ ) atomic unit] 0.53 Å, closing to  $\sim 0.45$  Å as probed with STM.

The small features at 7.1 eV appearing in the curves of 30–600 L coincide with that (sharp peak

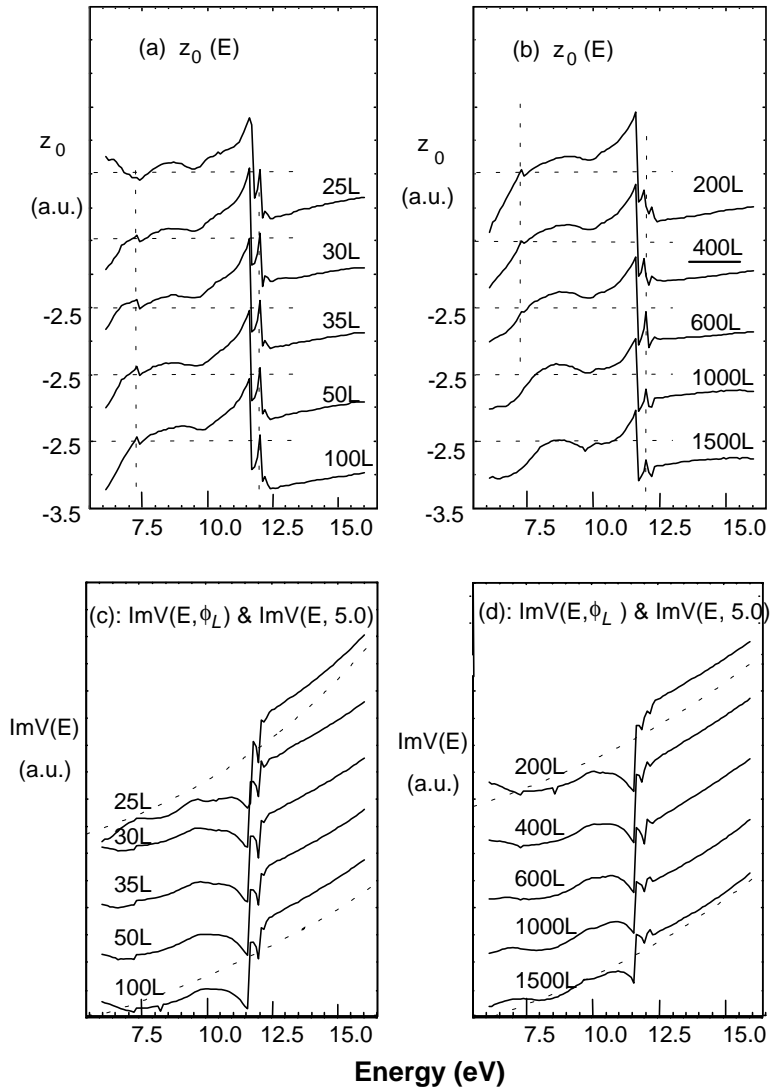


Fig. 14. Exposure-resolved  $z_0(E)$  (a, b) and  $\text{Im}V(E, \phi_L)$  (c, d) profiles exhibiting joint features of topography and spectroscopy provide duplication of the spectra in Figs. 13(a)–13(c). The  $z$  axis is directed into the bulk. The features on the  $z_0(E)$  curves ( $\leq 600$  L) at 7.1 eV coincide with those that appeared in STS.<sup>37</sup> Absence of the feature below 7.1 eV for 25 L indicates that  $\text{O}^{-1}$  dominates at this coverage. Violent features at 11.8–12.5 eV are attributed to the band-gap reflection. Broken lines represent the  $z_0$  value ( $-2.5$  a.u.) and the monotonic damping  $\text{Im}V(E, 5.0)$  for the pure Cu(001) surface. The general outward shift of the  $z_0(E)$  profiles corresponds to the reduction in the work function.<sup>35</sup>

at 2.1 eV below  $E_F$ ) probed with STS from the O–Cu-chain region and PES from O–Cu surfaces. The creation of new occupied states below 7.5 eV is identified as the contribution of nonbonding states, as a result of orbital hybridization of oxygen. Hence the absence of the features below 7.5 eV at 25 L implies that the sp hybridization has not occurred yet at this stage in which  $\text{O}^{-1}$  dominates without orbital

hybridization. The presence of the bonding features around  $-5$  eV below  $E_F$ , as resolved in PES, may go beyond the resolution of VLEED and be convoluted by the spatial effect. The absence of the 7.1 eV sharp features above 600 L oxygen exposure is the annihilation of the hybridization state by the spatial effect on the reflect intensity, i.e. the saturation and outward shift of the metal dipoles.

The violent features at 11.8–12.5 eV ( $\sim$  vacuum level) come from the band-gap reflection, and the surrounding features from electron excitation near band edges. The shape similarity of all the  $z_0(E)$  profiles at energies higher than 7.5 eV indicates that energy states at the bottom of the valence bands and even the deeper p band are less affected by the chemisorption. Therefore, the focus on the variation of valence states and its derivatives on the spectral features are on the correct track.

It should be noted that the VLEED data at 25 L could be simulated using the single  $(\sqrt{2} \times 2\sqrt{2})R45^\circ-2O^{-2}$  phase. The calculation result seems to conflict with the STM observations<sup>38</sup> (Fig. 1 of Part I) that confirmed the coexistence of clean Cu(001),  $c(2 \times 2)-2O^{-1}$  and the  $(\sqrt{2} \times 2\sqrt{2})R45^\circ-2O^{-2}$  phases at low oxygen exposures ( $< 25$  L). The extremely low damping of the clean Cu(001) in Subsec. 3.3 of Part I [ $\text{Im} V(E = 6.0 \text{ eV})$ ,  $\text{Im} V(E = 16.0) \cong (0.78, 0.81 \text{ eV})$ ], and the  $c(2 \times 2)-2O^{-1}$  (1.0, 3.0 eV),<sup>24</sup> indicates that information from these two phases has been filtered out by the high damping of the  $(\sqrt{2} \times 2\sqrt{2})R45^\circ-2O^{-2}$  phase (1.3, 6.5 eV). The high damping of the Cu<sub>3</sub>O<sub>2</sub> phase can be gained by substituting  $\gamma = -0.9703$ ,  $\delta = 6.4478$  and  $\phi_L \cong 4.0 \text{ eV}$  into the  $\text{Im} V(z, E)$  in Subsec. 2.4 of Part I. In fact, the relative number and the saturation degree of the dipoles dominate the intensity of the damping.  $O^{-1}$ -induced dipoles comprising the  $c(2 \times 2)-2O^{-1}$  domain boundaries should be less saturated than those induced by the lone pairs of  $O^{-2}$  in the  $(\sqrt{2} \times 2\sqrt{2})R45^\circ-2O^{-2}$  phase.

#### 5.4. Summary

As analyzed above, the O-Cu(001) bonding kinetics is quantified as follows (refer to the Appendix and Table 5):

- (i)  $\Theta_O \leq 30$  L: The dissociated oxygen forms one contracting ( $Q_1 = 12\%$ ) ionic bond with a Cu atom (labeled 1) on the surface. Meanwhile, metallic bonds break up and the missing row forms.  $DCu_x$  reaches 0.15 Å and  $\angle 1O2$  reaches  $94.0^\circ$ .  $O^{-1}$  is located above the surface and forms an off-centered pyramid with surface Cu atoms.
- (ii)  $30 \text{ L} > \Theta_O \leq 35$  L:  $O^{-1}$  forms the second contracting (increase  $Q_2$  from 0 to 4%) ionic bond with a Cu atom (labeled 2) in the substrates second layer, and as a result the  $O^{-2}$  penetrates into the bulk and evolves its position from the apical site of a tetrahedron to the center of a tetrahedron upon the second bond formation. Meanwhile,  $\angle 1O2$  increases from  $94.0^\circ$  to  $98.0^\circ$ .
- (iii)  $35 \text{ L} > \Theta_O \leq 200$  L: The angle  $\angle 1O2$  increases, resulting in the relaxation  $D_{12}$ , and simultaneously angle  $\angle 1O2$  increases from  $98.0^\circ$  to a saturation value of  $102.0^\circ$  while other parameters show little change.
- (iv)  $\Theta_O > 200$  L: The interaction between  $O^{-2}$  and the lone-pair-induced  $\text{Cu}^{\text{dipole}}$  develops, which dominates the reaction at higher exposure and long-term aging. Lone pairs push the dipoles outward, and as a result, pairing dipoles form and bridge over the missing row.  $DCu_x$  increases from 0.15 to a maximum 0.45 Å at about 800 L.

The variations of the structure-dependent  $z_0(E)$  profiles (Fig. 14) agree with the bonding kinetics. The features are summarized as follows:

- Features below 7.5 eV, particularly the small sharp peak at 7.1 eV, appearing in the 30–600 L curves, are derivatives of the nonbonding states of the  $O^{-2}$  hybrid.<sup>39</sup>
- The insignificant outward shift at higher exposures corresponds to the reduction of the work function that is caused by the development of the metal dipoles.
- The absence of the nonbonding states at 25 L corresponds to the  $O^{-1}$  effect without sp orbital hybridization, while at higher exposures the 7.1 eV feature is blurred by the development of the metal dipoles.
- Similarity of the exposure-resolved  $z_0(E)$  profiles at energies greater than 7.5 eV implies that chemisorption has little effect on the electrons at the bottom of the valence band or even deeper. The weak bonding states ( $\sim -5.0 \text{ eV}$ ) may go beyond the resolution of VLEED due to the spatial convolution by saturated  $\text{Cu}^{\text{dipole}}$ . Electron transportation occurs only involving the upper valence band of Cu.

A consistent understanding of the bonding kinetics and the corresponding variation of valence DOS has thus been obtained through both the bond geometry and the  $z_0(E)$  profiles, which provides further

evidence that the modeling approaches are substantially complete and realistic, and that the VLEED technique is unique and powerful in surface science.

## 6. Aging and Annealing Effect

### 6.1. Time-resolved VLEED data

VLEED  $I-E$  scans after aging and annealing of the specimen provide useful information about the bond formation under such conditions. Figure 15(a) shows the effect of annealing and aging on the VLEED  $I-E$  curves of a 300 L oxygen-exposed Cu(001) surface. The time-resolved spectra to be decoded were collected at  $72.0^\circ$  incidence and  $42.0^\circ$  azimuth.<sup>8</sup> The experimental conditions and the fine-structure features of these spectra are summarized as follows:

- Scan A was taken immediately after the clean Cu(001) surface was exposed to 300 L oxygen. There are two broad peaks, at 9.0 and 11.0 eV, and two sharp peaks, at 10.5 and 12.0 eV.
- Scan B was taken after 25 min of aging and produced the same result, apart from a change in the slope (it goes up) below 9.5 eV.
- Scan C was taken after 5 min of mild heating, to a dull red color, and showed a change in structure. Besides the slope below 9.5 eV, the whole spectrum increases in intensity.
- Scan D was taken after a further 3 h of aging. No change in structure from scan C is noted apart from a general attenuation in the intensity of the spectrum, and the intensity decreases significantly below 9.5 eV. The changes between scan C and scan D are similar in effect to the result of oxygen exposure greater than 200 L.

In general, the spectral shape and intensity below 9.5 eV are more sensitive to the aging and annealing, which indicates that reaction modifies energy states in the upper part of the valence band, as noted in the last section.

### 6.2. Dehybridization of oxygen

As a reference, the geometrical and SPB parameters for curve D in Fig. 15(a) were fixed first. The optimized  $z_0(E)$  profiles and the bulk damping  $\text{Im}V(E)$  for scans A–D are shown in Figs. 15(b) and 15(c), respectively. The corresponding structural parameters are given in Table 6. The calculation procedures are

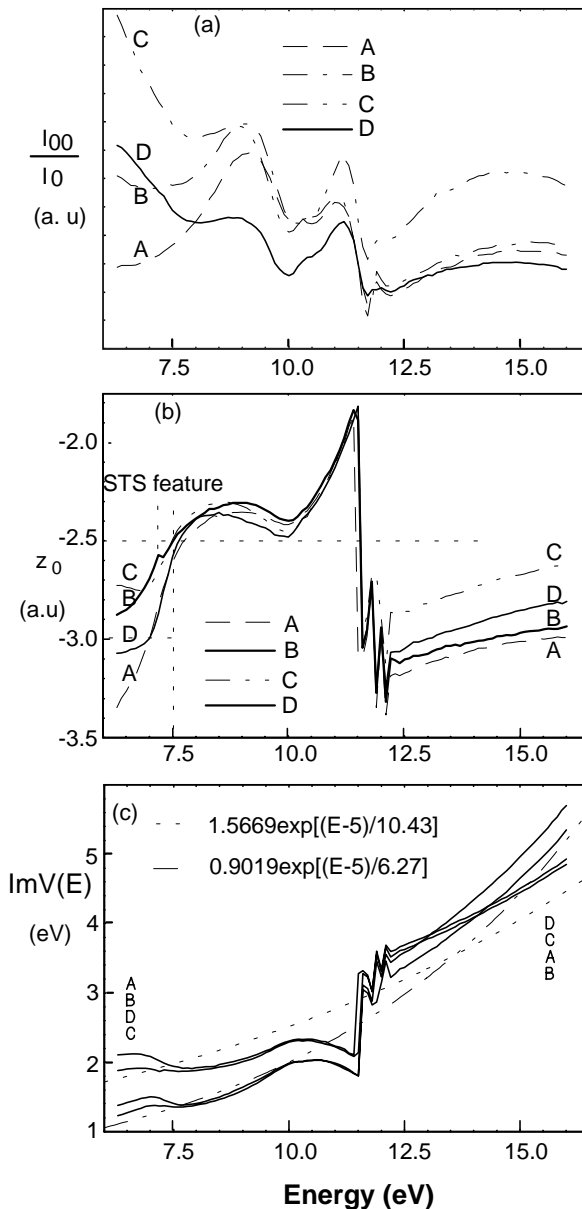


Fig. 15. Annealing and aging effect on the (a) VLEED spectra<sup>8</sup> and the corresponding (b) energy dependence of  $z_0(E)$  profiles and (c) the damping  $\text{Im}V(E)$ , which provide duplication of the VLEED spectra. Annealing increases the slope of the inelastic damping. Except for the  $z_0(E)$  of plot B, the hybridization feature at 7.1 eV is invisible for all the  $z_0(E)$  curves. The lowering of  $z_0(E)$  below 7.5 eV (lone-pair features) for scan C indicates the dehybridization of oxygen due to annealing.<sup>40</sup>

the same as that used in the previous section. First, a structure-sensitivity examination was performed based on the fixed parameters for curve D. Figure 16 shows the results of varying individual

Table 6. Cu<sub>3</sub>O<sub>2</sub> structure varies with aging and annealing of the O-Cu(001) surface.<sup>40</sup>

VLEED scans		A(g)	B(h)	C	D
Bond length (Å)	BL1	1.628	1.628	1.628	1.628
	BL2	1.776	1.776	1.776	1.776
	BL3	1.9053	1.9112	1.9202	1.9297
Bond angle (°)	BA12	101.00	101.25	101.50	102.00
	BA31	105.42	105.48	105.40	105.17
	BA32	96.83	95.52	98.77	100.03
	BA33	143.02	141.98	140.46	138.92
Atomic shift (Å)	DCu <sub>x</sub>	0.150	0.175	0.225	0.275
	DCu <sub>z</sub>	-0.0844	-0.1015	-0.1375	-0.1679
	DO <sub>x</sub>	-0.1852	-0.1858	-0.1864	-0.1877
	DO <sub>z</sub>	0.1442	0.1488	0.1553	0.1682
Layer spacing	D <sub>12</sub>	1.9086	1.9150	1.9215	1.9343
Damping	γ	1.5669		0.9019	
Potential	δ	10.427		6.2736	

Controlling variables are BA12 and DCu<sub>x</sub>. V<sub>0</sub> = 10.56 eV.

bond variables of BL2 ( $Q_2$ ), BA12 and DCu<sub>x</sub>. In comparison with the bond variable, DO<sub>z</sub> is also examined to establish the effect of individual atomic displacement. Calculated spectra indicate that the aging and annealing effect is not readily, as was the exposure effect, quantified by varying individual bond parameters except for the long-duration aging (from scan C to scan D). Spectra under long-duration aging can be simulated simply by changing DCu<sub>x</sub> alone. The results in Fig. 16 show us, however, that features below 9.5 eV in Fig. 15(a) can be modulated by the combination of BA12 and  $Q_2$ . Features in scan C, after 5 min of annealing, can be produced by reducing DCu<sub>x</sub>. The adjustment of DCu<sub>z</sub> produces no apparent variation of the spectrum that can match observed trends, and thus this is evidence again that the displacements of individual atoms are less realistic than the variation of bond geometry. From the structure-sensitivity examination, it is concluded that the time-resolved VLEED data can be simulated but the bonding kinetics appears not to be as explicit as that which happened in the processes of increasing oxygen exposure.

The  $z_0(E)$  and Im  $V(E)$  profiles in Figs. 15(b) and 15(c) vary their shapes apparently at energies outside 7.5–12.5 eV. Features below 7.5 eV corre-

spond to the nonbonding states of O<sup>-2</sup>. The  $z_0(E)$  features above 12.5 eV are dominated by inelastic damping. Apart from profile B, the small feature at 7.1 eV, the sp hybridization of oxygen, is absent from the  $z_0(E)$  profiles. This fact suggests that the sp hybridization is not fully developed yet immediately after the specimen is exposed (scan A) to oxygen, and that the dehybridization occurs due to annealing (scan C). The absence of the small feature from curve D is similar to that which happened to the O exposure greater than 600 L, due to the annihilation of the lone-pair features by the fully developed metal dipoles. The intensity of the hybridization states (< 7.5 eV) in curve C is obviously weakened. On the other hand, annealing treatment (for scans C and D) changes the slope of damping, as indicated in Fig. 15(c). At lower energies Im  $V(E)$  becomes lower while at higher energies it is higher. Features at energy lower than 7.5 eV imply that the energy states in the upper part of valence bands are more ready to be affected by annealing than the states at the bottom. The change of upper states corresponds to the formation of nonbonding lone pairs, namely the hybridization of O<sup>-2</sup>. The lower states correspond to the O-Cu bonding. Weakening the  $z_0(E)$  and Im  $V(E)$  features at lower

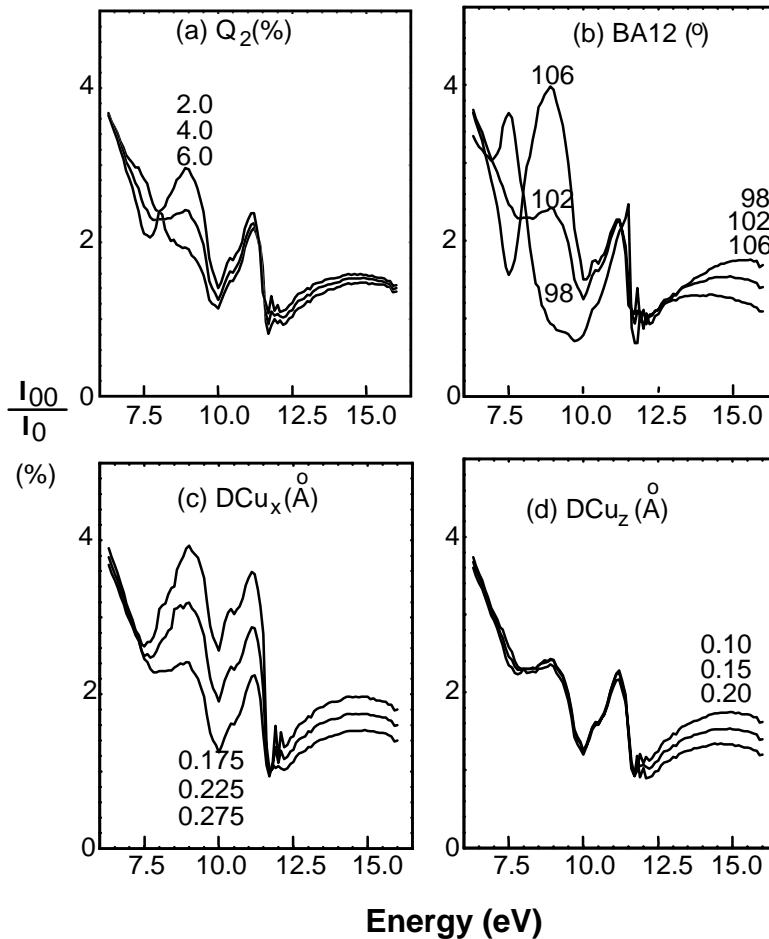


Fig. 16. Sensitivity of VLEED  $I-E$  scan D to bond geometry.<sup>40</sup> The results indicate that the aging and annealing effect is not readily quantified by individual bond parameters except for the long-duration aging [from scan C to scan D in Fig. 15(a)] which can be described by increasing  $DCu_x$  [panel (c)] alone. Features below 9.5 eV of scans A–D in Fig. 15(a) can be modulated by the joint contribution of  $Q_2$  [panel (a)] and BA12 [panel (b)].

beam energy due to annealing indicates that oxygen dehybridization takes place. Therefore, annealing supplies energy for oxygen to be dehybridized, which forms also the basis of thermal desorption and bond switching of oxide tetrahedron.<sup>41,42</sup>

### 6.3. Precursor confirmation

As far as the structure of the precursor phase [scan A in Fig. 15(a)] is concerned, eight different structures were compared by  $z_0$ -scanning calculations. The reason for the comparison is that the aging and annealing processes are less affirmative and thus it is necessary to inspect other possible structures. Supposing oxygen and copper were in the ideally metallic

or ionic states and it were true that oxygen bonds to its four neighbors identically, then models (a) and (b) would be a centered pyramid  $c(2 \times 2)-2O^{-1}$  structure ( $DO_x = 0$ ) with four identical bond lengths of 1.96 Å (metallic) and 1.85 Å (ionic), respectively. Models (c), (d) and (e) are off-centered pyramid structures ( $DO_x \neq 0$ ) with one O–Cu ionic bond which contracts by 3%, 4% and 12%, correspondingly. Model (f) is similar to (e) but  $DO_z$  decreases from 0.30 to 0.15 Å. The structural parameters of the six models are controlled by  $DO_z$  and BL1, as listed in Table 7. Models (g) and (h) are the current  $Cu_3O_2$  structures optimized for scans A and B as given in Table 6. As the yields of the  $z_0$ -scanning calculations, the  $z_0(E)$  plots are compared in Fig. 17.

Table 7. Structure parameters for the confirmation of the precursor state.<sup>40</sup>

Model		a	b	c	d	e	f
Atomic shifts	$DO_x$	0.0	0.0	-0.0869	-0.0743	-0.1454	-0.1305
	$DO_z$	-0.7592	-0.3965	-0.5115	-0.3895	-0.30	-0.15
Bond length	BL1	1.960	1.850	1.795	1.776	1.628	1.628
	BL2	1.960	1.850	1.880	1.850	1.970	1.940
Inelastic potential	$\gamma$	1.6471	2.1418	1.8740	2.1418	2.6380	2.6380
	$\delta$	21.461	26.378	19.977	36.378	31.275	31.275

Parameters are controlled by BL1 and  $DO_z$ .  $D_{12} = 1.7889$  (contracting by 1%).  $DO_x = 0.0$  Å corresponds to a centered pyramid with four identical O-Cu bonds, otherwise an off-centered pyramid with one contracting ionic bond.  $V_0 = 11.56$  eV.

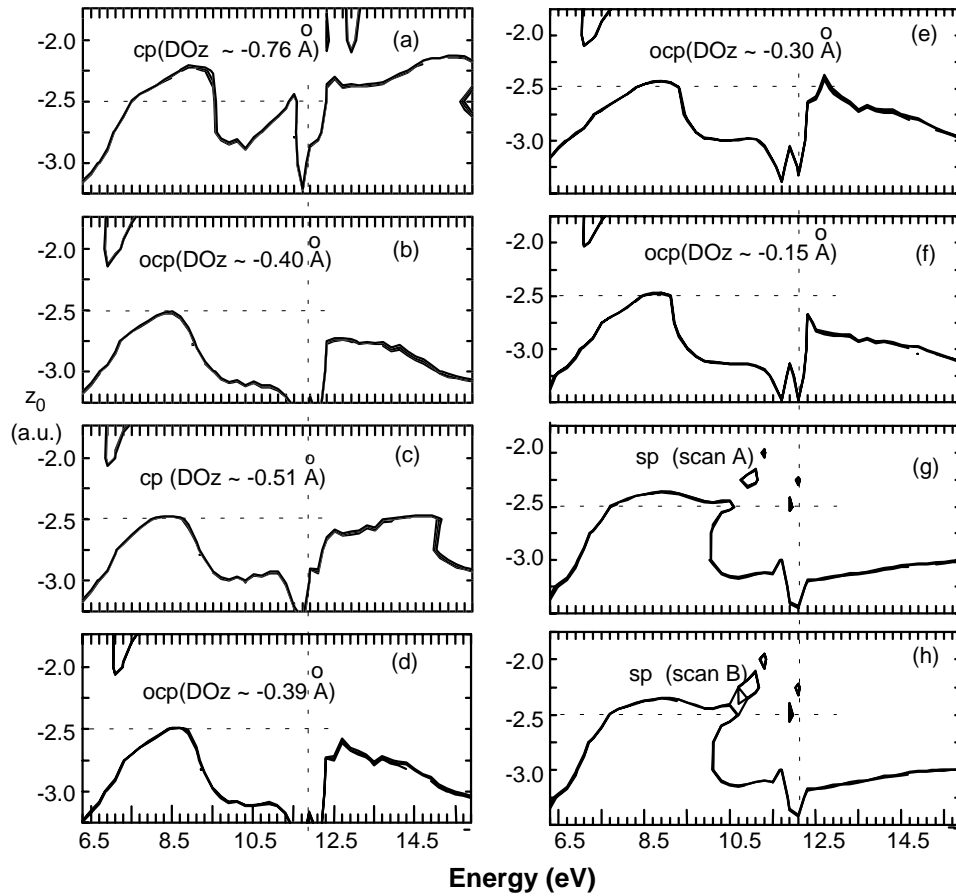


Fig. 17.  $z_0$ - $E$  contour plots of different structures for scan A.<sup>40</sup> Structural parameters are listed in Table 11. (a) and (b) result from centered-pyramid (cp)  $c(2 \times 2)$ -2O structures with four identical O-Cu bond lengths of 1.96 (metallic) and 1.85 Å (ionic). (c) and (d) correspond to an off-centered pyramid (ocp) with one O-Cu ionic bond contracting by 3% and 4%. (e) and (f) result from an off-centered pyramid with one O-Cu bond contracting by 12% but with different  $DO_z$ . (g) and (h) correspond to the  $Cu_3O_2$  structure (sp) optimized for scans A and B as given in Table 6.

Table 8. CN dependence of the O–Cu metallic (A–D) bond length and  $DO_z$  (Å) obtained on the premise of a centered pyramid with four identical O–Cu bonds.<sup>40</sup>

	$R_O$	$R_{Cu}$	$D_{O-Cu}$	$DO_z$
A	0.66 (CN = 12)	1.276 (CN = 12)	1.936	0.6949
B	0.66	1.173 (CN = 1)	1.839	0.3076
C	0.74 (CN = 1)	1.276 (CN = 12)	2.016	0.8939
D	0.74	1.173 (CN = 1)	1.913	0.6279
E (ionic)	1.32	0.53	1.85	0.3965

All the  $z_0(E)$  profiles in Fig. 17 correspond to the matching fit of the measured data of scan A in Fig. 15(a). The shapes of the  $z_0(E)$  curves, however, vary obviously with atomic positions. In the  $z_0$ -scanning method, determination of the structure models was carried out by comparing the shapes of the contour plots of  $z_0(E)$ . The interdependence between the crystal structure and the corresponding  $z_0(E)$  profile allows us to judge a reasonable structure from the infinite number of mathematical solutions by properly setting up criteria for the shape of the  $z_0(E)$  profile. Referring to the constraints on  $z_0(E)$  curves established in Subsec. 3.1 of Part I, models (a) and (c), with oxygen located higher than 0.4 Å above the unreconstructed top layer, are excluded first due to the roughness of the  $z_0(E)$  curves. Models (b), (d) and (e), with oxygen 0.3–0.4 Å above the Cu surface, smoothen the  $z_0(E)$  curves similarly but the  $z_0$  around 12.5 eV is too low. The low  $z_0$  around 12.5 eV disagrees with the band transition mechanism that adds a hump to the damping and correspondingly to the  $z_0(E)$  curve. Models (g) and (h) are preferred though they give multiple solutions within 10.3–12.0 eV, which cannot be avoided in all the missing-row structures. However, the comparison implies that in the precursor stage an off-centered-pyramid structure, with one contracting ionic bond and  $DO_z < 0.4$  Å, is most likely. This identity agrees with what was revealed with STM and confirmed by the exposure-resolved VLEED.

The value of  $DO_z \leq 0.4$  Å should be true on the premise of surface bond contraction. Generally, an atom contracts its radius with the reduction of its CN regardless of the nature of the bond (Subsec. 2.1 of Part I). Given that oxygen and copper atoms were rigid spheres and the oxygen bonded to its four Cu

neighbors equally, the possible O–Cu bond lengths and the corresponding values of  $DO_z$  are compared in Table 8. The CN of the atom in the top layer is between 1 and 12, so that the maximal (C: 2.016 Å) and minimal (B: 1.839 Å) metallic bond lengths are excluded. The metallic bond length estimated at  $1.925 \pm 0.010$  Å agrees with what was determined by other means. If B and C are excluded as reasoned above, the possible  $DO_z$  in the metallic-bond model is  $0.66 \pm 0.04$  Å. Assuming that four identical ionic bonds with covalent contribution form without bond contraction, the  $DO_z$  of the centered pyramid is calculated as  $\sim 0.4$  Å (refer to E in Table 8).

It should be emphasized that oxygen possesses no more than two bonding orbitals. Upon sp-orbital hybridization, half of the four directional orbitals are occupied by bonding electron pairs, and the other half by nonbonding lone pairs. Therefore, it is not realistic for oxygen to bond identically with the four neighbors in a surface plane. On the other hand, the difference in electronegativity ( $\Delta\chi = 1.8$ ) between oxygen and copper determines the nature of O–Cu bonding to be mainly ionic. No covalent, metallic or even antibond between oxygen and copper are permitted as they are subject to the  $\Delta\chi$  criterion ( $\gg 2$ ). Forming the antibond requires extra energy higher than that for the nonbonding lone pairs. Therefore, the acceptable solution for the precursor state is the off-centered pyramid with an oxygen located lower than 0.4 Å above the Cu(001) surface, as justified with the  $z_0$ -scanning calculations mentioned above. It can be understood that in the precursor phase oxygen forms one contracting ionic bond with one copper atom, rather than four identical bonds with its surface neighbors in the same plane, as quantified in Sec. 2.

Briefly, the effect of aging and annealing on the O-Cu(001) system is slightly complex and therefore it is less explicit than the effect of increasing oxygen exposure. However, it is certain that long-term aging has the same effect as higher oxygen exposure on the spectral features that can be understood as the development of interaction between the nonbonding lone pairs and the lone-pair-induced Cu<sup>dipole</sup>. It is also found that the annealing provides a force to dehybridize the oxygen, reducing  $DCu_x$  and the DOS features of lone pairs rather than enhancing the bond formation. The preferred precursor is the off-centered pyramid as confirmed with STM.

## 7. Summary

The kinetic VLEED, furnished with the decoding technique and the models, has enabled us to gain a comprehensive insight into the nature and kinetics of oxide bond forming and its consequences for the behavior of atoms and valence electrons on the Cu(001) surface from the perspective of bond geometry, valence DOS and the 3D SPB. The ways of extracting information from the combination of STM, PES and the kinetic VLEED are proven to be definitive, complete and essentially correct, showing that our approaches reflect the real process of reaction and the natural correlation among the parameters and the known identities. The major progress made is summarized as follows:

- The bond model with a small number of parameters and physical constraints represents the real situation in which atoms move their positions collectively. Atomic dislocation and surface relaxation are driven by the bond geometry. The model indicates that oxidation is a kinetic process of electron transportation in which O<sup>-1</sup> forms first and then O<sup>-2</sup> follows with sp-orbital hybridization and lone-pair production. O<sup>-2</sup> prefers a location in the near-center of a tetrahedron. Importantly, O<sup>-1</sup> or the nonbonding lone pair induces metal dipoles at the surface. Besides the electron transportation between the oxygen and metals, the metal dipoles as well as the nonbonding states of the hybridized O<sup>-2</sup> play a key role in the electronic processes and physical properties of oxidation. For example, the strongly localized electrons with low mobility reduce the work function but increase the contact electrical resistance.

- As a consequence of bond forming, oxygen derives additional valence-DOS features of O-M bonding, nonbonding lone pairs of oxygen, antibonding metal dipoles and the holes around  $E_F$ . Therefore, oxygen possesses the special capacity to create a gap or widen the existing band gap, and add a sub-band above  $E_F$  reducing the work function, which agrees with the PE detection of a number of metal surfaces with chemisorbed oxygen. Oxidation formulates the surface atomic valences, which relate to the STM signatures.
- The single-variable parametrized SPB functions uncover the full capacity of VLEED in simultaneously determining the bond geometry, the shape of the SPB and the variation of the valence DOS, and their interdependence. One can judge models by simply comparing the shapes of the geometrically-dependent  $z_0(E)$  curves.
- O-Cu(001) reaction is a kinetic process that progresses in four discrete stages. The Cu<sub>3</sub>O<sub>2</sub> configuration indicates that one Cu may donate more than one electron to different oxygen adsorbates but one oxygen atom cannot get more than one electron from a specific Cu. This provides the basis of preferential oxidation of a certain orientation of crystalline such as diamond {111} faces.<sup>42</sup>
- The O-Cu(001) surface bond forming is responsible for all the observations, whether static or kinetic. Bond geometry determines atomic dislocation and surface relaxation. The strong localization of surface electrons and variation of the energy states, as well as the reduction in both the work function and the inner-potential constant, result from the electron transportation from one energy level to the other, such as polarization and ionization of different atoms. It is emphasized that the bonding effect is readily detectable while the process of electron transportation is beyond the capacity of currently popular means.
- VLEED is such a unique technique that it collects quantitative and nondestructive information from a single atomic layer and covers the valence-band range of a surface regarding the bond geometry, the bond-forming kinetics and the corresponding change of atomic dislocations, valence DOS and the surface potential. VLEED enables the current modeling approach to be verified and the modeling approach, in turn, uncovers the full capacity and reliability of the VLEED technique.

• Importantly, this work reveals two essential events occurring at a surface. One is the *surface bond contraction* and the other is the *sp-orbital hybridization with lone-pair and dipole formation*. The spontaneous bond contraction leads to a change of the binding energy and their derivatives. Surface bond contraction and the rise in the surface-to-volume ratio have been found to be responsible for the size dependency of nanometric solids, such as lattice contraction,<sup>43</sup> enhancement of surface stress and Young's modulus,<sup>44,45</sup> band-gap expansion<sup>46,47</sup> and dielectric suppression of nanometric semiconductors<sup>48</sup> and diamond<sup>49,50</sup> melting-point rise or depression, enhancement of magnetization, modification of the phase-transition temperature of PZT materials.<sup>51,52</sup> The extension of sp-orbital hybridization to the bonding of C, N and O to the fcc(001) surface of Rh and Ni, which has led to a new approach, improving the adhesion between diamond and metals.<sup>53</sup> The band-gap-generating mechanism has led to the finding that the PbZrTi oxide emits intensive blue light.<sup>54</sup> Applying the knowledge to the interaction of O with the fcc{(001), (110), (111)} surfaces of Cu and Rh,<sup>55</sup> as well as the hcp{(10 $\bar{0}$ ), (0001)} of Ru<sup>56</sup> and Co,<sup>57,58</sup> has led to a consistent understanding of the multiphase reaction kinetics observed by means of STM,<sup>59,60</sup> LEED,<sup>61</sup> PES and TDS,<sup>62</sup> which prompts the conclusion<sup>63</sup> that though the surface morphologies, atomic geometries and phase ordering may vary from case to case, the basic oxide tetrahedron, the oxygen-derived DOS features and the kinetics of bond forming are substantially the same in all the considered cases. The various observations are consequences of bond formation that depends on the electronegativity, atomic size and lattice geometry of the host surface differing from case to case, and the controlling parameters seem not surprisingly to be temperature, oxygen exposure and aging time.

It would be more challenging and rewarding to apply the approaches and the derivatives for new and important findings in fields such as catalytic electronics, bioelectronics, magnetoelectronics and photoelectronics, as well as functional materials and nanotechnology.

## Acknowledgments

I am grateful to Profs. P. Jennings, S. Thurgate, A. Stelbovics and G. Hitchen for providing me with the VLEED data and code as well as their valuable communications, which enabled the progress presented. I would like to express my sincere thanks to Profs. S. Y. Tong, A. T. S. Wee, K. P. Loh, C. L. Bai and E. Jiang for helpful discussions. Critical reading and editorial instructions by Prof. S. Y. Tong, and kind endorsement of the related works linked to this presentation by Profs. M. Donath, S. Tear, G. Russell, L. A. Bursill, L. Holland, O. S. Heavens and A. Mookerjee, are all gratefully acknowledged.

## Appendix

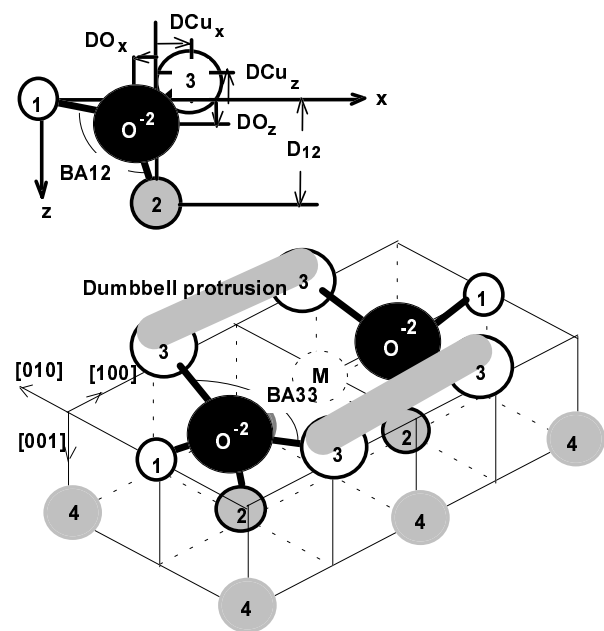
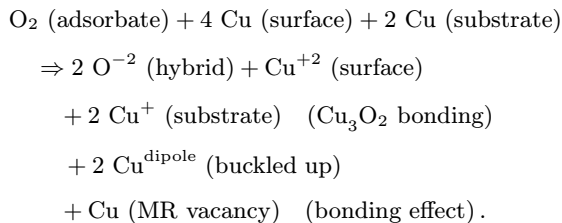


Fig. 1.  $\text{Cu}_3\text{O}_2$  pairing tetrahedron models the Cu(001)- $(2\sqrt{2} \times \sqrt{2})\text{R}45^\circ\text{-}2\text{O}^{-2}$  reconstruction:



$\text{O}^{-2}$  prefers the center of a quasi-tetrahedron. Atoms 1 and 2 are  $\text{Cu}^{+2}$  and  $\text{Cu}^+$ . Atom 3 is  $\text{Cu}^{\text{dipole}}$  and M is the vacancy of the missing Cu arisen due to the isolation of this atom. Atom 4 is the metallic Cu atom. The pairing dipoles 3-3 cross over the missing row.

## References

1. C. Q. Sun, *Surf. Rev. Lett.* **8**(3/4), 367 (2001).
2. V. Pouthier, C. Ramseyer, C. Girardet, P. Zeppenfeld, V. Diercks and R. Halmer, *Phys. Rev.* **B58**, 9998 (1998).
3. C. Q. Sun and C. L. Bai, *J. Phys. Chem. Solids* **58**, 903 (1997).
4. C. Q. Sun *et al.*, *Int. J. Mod. Phys. B*, in press.
5. R. Mayer, C. Zhang and K. G. Lynn, *Phys. Rev.* **B33**, 8899 (1986).
6. T. Lederer, D. Arvanitis, G. Comelli, L. Troger and K. Baberschke, *Phys. Rev.* **B48**, 15390 (1993).
7. C. Q. Sun, *Vacuum* **48**, 491 (1997).
8. G. Hitchen, S. M. Thurgate and P. Jennings, *Aust. J. Phys.* **43**, 519 (1990).
9. G. Hitchen and S. Thurgate, *Phys. Rev.* **B38**, 8668 (1988).
10. G. Hitchen and S. Thurgate, *Surf. Sci.* **197**, 24 (1988).
11. M. A. Omar, *Elementary Solid State Physics: Principles & Applications* (Addison-Wesley, 1975).
12. C. Kittel, *Introduction to Solid State Physics*, 5th ed. (Wiley, New York, 1976).
13. R. O. Jones and P. J. Jennings, *Surf. Sci. Rep.* **9**, 165 (1988).
14. E. G. McRae and C. W. Caldwell, *Surf. Sci.* **57**, 766 (1976).
15. C. Q. Sun, *Int. J. Mod. Phys.* **B11**, 3073 (1997).
16. H. C. Zeng, R. A. McFarlane, R. N. S. Sodhi and K. A. R. Mitchell, *Can. J. Chem.* **66**, 2054 (1988).
17. R. A. DiDio, D. M. Zehner and E. W. Plummer, *J. Vac. Sci. Technol.* **A2**, 852 (1984).
18. U. Döbler, K. Baberschke, J. Stöhr and D. A. Outka, *Phys. Rev.* **B31**, 2532 (1985).
19. K. W. Jacobsen and J. K. Nørskov, *Phys. Rev. Lett.* **65**, 1788 (1990).
20. J. M. Baribeau, J. Lopez and J. C. Le Boss, *J. Phys.* **C18**, 3083 (1985).
21. S. Warren, W. R. Flavell, A. G. Thomas, J. Hollingworth, P. L. Wincott, A. F. Prime, S. Downes and C. Chen, *J. Phys. Cond. Matt.* **11**, 5021 (1999).
22. P. J. Jennings and S. M. Thurgate, *Surf. Sci.* **104**, L210 (1981).
23. J. Rundgren and G. Malmstrom, *Phys. Rev. Lett.* **38**, 836 (1977).
24. S. M. Thurgate and C. Q. Sun, *Phys. Rev.* **B51**, 2410 (1995).
25. H. Pfnür, M. Lindroos and D. Menzel, *Surf. Sci.* **248**, 1 (1991).
26. P. Hofmann, R. Unwin, W. Wyrobisch and A. M. Bradshaw, *Surf. Sci.* **72**, 635 (1978).
27. C. Benndorf, B. Egert, G. Keller and F. Thieme, *Surf. Sci.* **74**, 216 (1978).
28. C. Benndorf, B. Egert, B. Keller, H. Seidel and F. J. Thieme, *Phys. Chem. Solids* **40**, 877 (1979).
29. L. H. Dubois, *Surf. Sci.* **119**, 399 (1982).
30. G. Ertl and T. N. Rhodin, *The Nature of Surface Chemical Bond* (North-Holland, 1979).
31. J. Lauterbach and H. H. Rotermund, *Surf. Sci.* **311**, 231 (1994).
32. H. H. Rotermund, *Surf. Sci.* **283**, 87 (1993).
33. F. Jensen, F. Besenbacher, E. Lagsgaard and I. Stensgaard, *Phys. Rev.* **B42**, 9206 (1990).
34. C. Q. Sun, *Vacuum* **48**, 865 (1997).
35. C. Q. Sun, *Vacuum* **48**, 535 (1997).
36. M. Wuttig, R. Franchy and H. Ibach, *Surf. Sci.* **224**, L979 (1989).
37. F. M. Chua, Y. Kuk and P. J. Silverman, *Phys. Rev. Lett.* **63**, 386 (1989).
38. T. Fujita, Y. Okawa, Y. Matsumoto and K. Tanaka, *Phys. Rev.* **B54**, 2167 (1996).
39. C. Q. Sun and S. Li., *Surf. Rev. Lett.* **7**, L213 (2000).
40. C. Q. Sun, *Vacuum* **48**, 525 (1997).
41. C. Q. Sun and S. Li, *Surf. Rev. Lett.*, in press.
42. C. Q. Sun, H. Xie, W. H. Zhang, H. Ye and P. Hing, *J. Phys.* **D33**, 2196 (2000).
43. C. Q. Sun, *J. Phys. Cond. Matt.* **11**, 4801 (1999).
44. C. Q. Sun, B. K. Tay, S. P. Lau, X. W. Sun, X. T. Zeng, H. Bai, H. Liu, Z. H. Liu, E. Y. Jiang, *J. Appl. Phys.* **90**, 2615 (2001).
45. C. Q. Sun, B. K. Tay, S. P. Lau and X. W. Sun, *SPIE Proc.* **4228**, 302 (2000).
46. Sun C. Q., X. W. Sun, H. Q. Gong, H. Huang, H. Ye, D. Jin and P. Hing, *J. Phys. Cond. Matt.* **11**, L547 (1999).
47. C. Q. Sun, H. Q. Gong, P. Hing and H. T. Ye, *Surf. Rev. Lett.* **6**, L171 (1999).
48. C. Q. Sun, X. W. Sun, B. K. Tay, S. P. Lau, H. Huang and S. Li, *J. Phys.* **D34**, 2359 (2001).
49. C. Q. Sun, H. T. Ye, H. T. Huang and P. Hing, *Appl. Phys. Lett.* **78**, 1826 (2001).
50. H. T. Ye, C. Q. Sun and P. Hing, *J. Appl. Phys.* **D33**, L148 (2000).
51. H. Huang, C. Q. Sun and P. Hing, *J. Phys. Cond. Matt.* **12**, L127 (2000).
52. H. Huang, P. Hing, C. Q. Sun and T. S. Zhang, *Phys. Rev.* **B63**, 184112 (2001).
53. C. Q. Sun, *Surf. Rev. Lett.* **7**, 347 (2000).
54. C. Q. Sun, D. Jin, J. Zhou, B. K. Tay, S. P. Lau, X. W. Sun, H. T. Huang and P. Hing, *Appl. Phys. Lett.* **79**, 1082 (2001).
55. C. Q. Sun, *Surf. Sci.* **398**, L320 (1998).
56. K. Meinel, H. Wolter, C. Ammer, A. Beckmann and H. J. Neddermeyer, *Phys.: Cond. Matter.* **9**, 4611 (1997).
57. R. Koch, E. Schwarz, K. Schmidt, B. Burg, K. Christmann and K. H. Rieder, *Phys. Rev. Lett.* **71**, 1047 (1993).
58. C. Q. Sun, *Surf. Rev. Lett.* **5**, 1023 (1998).

59. S. Schwegmann, A. P. Seitsonen, H. Dietrich, H. Bludau, H. Over, K. Jacobi and G. Ertl, *Chem. Phys. Lett.* **264**, 680 (1997).
60. R. Koch, B. Burg, K. Schmidt, K. H. Rieder, E. Schwarz and K. Christmann, *Chem. Phys. Lett.* **220**, 172 (1994).
61. S. Schwegmann, H. Over, V. De Renzi and G. Ertl, *Surf. Sci.* **375**, 91 (1997).
62. K. Yagi, K. Higashiyama and H. Fukutani, *Surf. Sci.* **295**, 230 (1993).
63. C. Q. Sun, "Oxidation Electronics," to be published.